
Akkretierende Neutronensterne

Zeitliche Entwicklung der Pulsperiode von 4U 1907 + 09

Bachelorarbeit

vorgelegt von
Bastian Falkner

Erlangen Centre for Astroparticle Physics
Dr. Remis-Sternwarte Bamberg
Friedrich-Alexander-Universität
Erlangen-Nürnberg

1. Gutachter: Prof. Dr. Jörn Wilms & Dr. Ingo Keykenbohm
2. Gutachter: Prof. Uli Heber

Tag der Abgabe: 28.09.2010

Abstract

I investigate the accretion powered High Mass X-ray Binary 4U 1907 + 09. Based on 21 observations with a total exposure time of 34 ks provided by the proportional counter array (PCA) on board of the Rossi X-ray Timing Explorer (*RXTE*) it was attempted to calculate the pulse period evolution in the epoch from 54705.4 MJD and 55387.8 MJD. In continuation to the results of Inam et al. (2009) also the phase connection method was used, but failed to find a consistent model. An attempt to compensate the lack of a proper reference period by variate it also failed. Therefore the conclusion is that there is a major change in the pulse period evolution, i.e. the real pulse period deviates from the model and accordingly from the predicted progression of Inam et al. (2009). Also another torque reversal is possible.

Contents

1	Introduction	3
2	The Rossi X-ray Timing Explorer (<i>RXTE</i>)	13
3	Observation and data reduction	15
4	Data analysis	20
4.1	Phase connection	20
4.2	Automated phase correction	28
4.3	Variation of the reference pulse period	28
5	Conclusions	34
A	Appendix	35
	Bibliography	44
	Acknowledgments	45

1 Introduction¹

The main objective of this bachelor thesis is to estimate the pulse periods of the X-Ray binary 4U 1907 + 09 in the period of August 2008 until July 2010 using data from the Rossi X-ray Timing Explorer (*RXTE*). To some extent this is the continuation of the measurements of Inam et al. (2009). In the first section an overview of binary systems and in particular of 4U 1907 + 09 is given. After presenting the used observation instrument (*RXTE/PCA*) in section 2 the data reduction and selection is discussed (section 3). Afterwards in section 4 the main analysis method (phase connection) will be explained and applied to 4U 1907 + 09 followed by the attempt to approach a problem occurring during the analysis. This Thesis closes with a summary of its conclusions in section 5.

4U 1907 + 09 is a High Mass X-ray Binary (HMXB), which was discovered by the *Uhuru* survey (Giacconi et al., 1971), consisting of a neutron star and a main sequence companion star. It has evolved from a binary star system, in which the more massive star has undergone the main sequence much faster than its companion and finished its life in a supernova, leaving today's neutron star behind.

There are several possible ways for the creation of a neutron star in a binary system, but the most likely scenario for 4U 1907 + 09 is a supernova of type II, which requires a progenitor with a mass of at least $8 M_{\odot}$ and less than $20 M_{\odot}$ (Smartt, 2009). In the final stages of its evolution the progenitor grows and may exceed its Roche lobe causing a mass transfer onto the companion star. The size of the Roche lobe depends on the mass ratio, the distance between the two stars, and the angular velocity. Only if the core of the progenitor still has a mass of more than $3 M_{\odot}$ the supernova explosion can take place. In this case most of the remaining stellar mass composing the envelope is blown away during the supernova explosion itself leaving only the collapsed core mainly consisting of neutrons generated by the inverse β decay. This neutron star usually has a mass of $1.4 M_{\odot}$ inside a radius of 10 km and a mean density of $10^{14} \text{ g cm}^{-3}$. Further important characteristics are its magnetic field, which is the conserved magnetic field of the progenitor shrunk into the neutron star and therefore can be very strong (up to 10^{12} G), for 4U 1907 + 09 it is $2.1 - 2.5 \cdot 10^{12} \text{ G}$ (Cusumano 1998). Its angular momentum is also conserved and accordingly its rotation period lying in broad regime from milliseconds to a few minutes, which will be discussed later in more detail and is around 440 s for 4U 1907 + 09. But there are still many open question, e.g. the detailed structure of neutron stars, which is suggested to consist of a more or less solid crust and a superfluid core.

4U 1907 + 09 is a persistent accretion-powered X-ray source in an eccentric ($e = 0.28$) Orbit of 8.38 days (in 't Zand et al., 1998) around its companion. To see X-ray emission there must be a mass transfer onto the neutron star, which is provided by the companion. This transfer can be due to different ways. As already mentioned it is possible that the companion can overflow its Roche lobe, i.e. the material of the outer layers are not gravitationally bound to the star anymore and will fall into the potential trough of the compact object. This mass transfer happens by forming a material stream over the inner Lagrangian point. But this material can not be captured directly by the compact object due to the angular momentum given by the donor star and hence an accretion disk will be developed. In that disk the angular momentum is dissipated through viscous

¹Unless otherwise noted the content of this section is based on Kreykenbohm (2004)

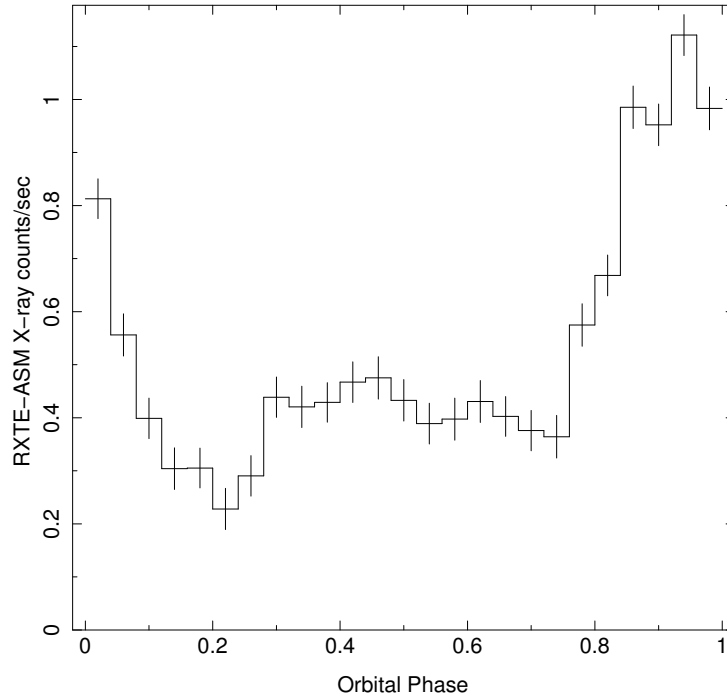


Figure 1: Double peaked orbital light curve of 4U 1907 + 09 calculated with the period fold method using an orbital period of 8.3757 d and a zero phase at periastron (Kostka & Leahy, 2010) based on data from the RXTE All-Sky Monitor (1.0 – 12.1 keV) in the epoch from 50088.38 until 55439.53 MJD.

motion, i.e. it is transported outward and radiated away.

Another mass loss process is the stellar wind, which is most intense for massive stars and is $7 \cdot 10^{-6} M_{\odot} \text{ yr}^{-1}$ for the companion of 4U 1907 + 09 (Fritz et al., 2006). As a first approximation this wind is emitted spherically symmetric, so that only a tiny fraction can be captured by the compact object, which, however, is enough to explain the observed luminosities. This factor, usually in order of 0.01 % of the mass loss of the star, is dependent on the size of the donator star, i.e. for increasing radius the fraction is decreasing, the mass ratio of the two stars and their binary separation. Not only the material that directly moves towards the compact object, but also material in a certain radius around it gets accreted, where its gravitational pull masters the momentum of the wind. Because there is also angular momentum involved, the formation of an accretion disk is not unlikely, even though the detailed structure is very complex and differs from that of the Roche lobe (see Bondi & Hoyle (1944) for detailed description of this mechanism). Although this process is very inefficient, the small fraction of material, which gets captured by the compact object exhibits a sufficient amount of energy to power the X-ray source.

Another way to achieve a sufficient mass transfer is attributed to a so called Be-stars. Those stars are very fast rotating, which arise from the angular momentum captured with the material of the progenitor of the compact object during its evolution, in which it had exceeded the Roche lobe. This fast rotation is believed to cause the formation of an equatorial decretion torus enlarging the effective radius of the star in the equatorial plane. Due to an eccentric orbit of the compact object it can transit that torus at its periastron and therefore accrete material. Additionally it is possible that a combination or even all three of the processes above are taking place simultaneous.

The companion of 4U 1907 + 09 was first thought to be a Be-star due to the two orbital phase locked peaks seen in the light curve in Figure 1. The stable and bright primary flare is locked to an orbital phase near periastron, the secondary near apastron and varies from orbit to orbit in a large range and is less significant than the primary. Makishima et al. (1984) suggested that this is due to a slightly inclination angle of the neutron star relative to the decretion torus of the companion. Assuming that the binary separation is less than the distance to the two intercept points of those planes these are two potential traverse points, which are leading to the observed periodic increase in the light curve. The eccentric orbit then explains the difference in brightness, i.e. the primary traverse point is closer to the star than the the second one compared to two identical flares with a none eccentric orbit. This explanation was supported by the observed strong H α emission line typical for Be-stars.

However, Cox et al. (2005) have shown that the companion of 4U 1907 + 09 is more likely to be a O8-O9 Ia supergiant and determined an effective temperature of 30500 K, a radius of $26 R_{\odot}$ and a luminosity of $5 \cdot 10^5 L_{\odot}$. They also estimated the distance to the binary system to be ~ 5 kpc excluding the possibility of the Be-star scenario, which would requiring a distance smaller than 1.5 kpc. Furthermore the huge mass loss rate of the stellar companion is of the order of a magnitude larger than the typical rate for Be-stars. This theory, however, does not answer the question for the reason for the double peaked light curve.

Kostka & Leahy (2010) however, came up with another suggestion for such a double peaked light curve. They considered a stream and wind model, which, in contrast to wind and disk models, could explain the periodic modulation of the light curve. Their model was also able to explain the light curve of the HMXB GX 301-2 (Leahy & Kostka, 2008), which is sufficiently comparable to 4U 1907 + 09. That model describes a stream, which originates at the closet point to the neutron star on the surface of the stellar companion (Fig. 2).²

The stream model is calculated by accounting the radial and azimuthal velocity of the stream, in which the radial velocity is assumed to follow the same profile as the stellar wind and the azimuthal velocity is given by orbital angular velocity, which varies due to the eccentric orbit. With respect to the direction of the orbital velocity the stream bends backwards like the water stream of an unevenly rotating sprinkler. It is also comparable to a corotating Archimedes spiral. The opening angle of the stream increases as the stellar wind velocity increases or the orbital angular momentum decreases. The stream itself spreads with a constant velocity and is assumed to have a Gaussian density profile. Applying this model to the light curve of 4U 1907 + 09 (Fig. 3), the luminosity dip at phase ~ 0.15 is due to the maximal separation of the neutron star and the accretion stream. Towards phase ~ 0.3 the stream catches up, but does not pass causing the extended peak seen between phase 0.3 and 0.7. As the neutron star accelerates towards periastron traveling down the accretion stream, i.e. increasing stream and wind density, the luminosity rises again peaking at a phase of 0.95. Also notable is the uneven influence of the wind and the stream model, which contributes almost all the luminosity.

Having discussed the mass transfer mechanisms, the accretion process onto the neutron star itself will be analyzed. Dealing with plasma and strong magnetic fields as for 4U 1907 + 09 with $2.1 - 2.5 \cdot 10^{12}$ G, it is essential to take it into account. As mentioned the

²A full simulated movie for the HMXB GX 301-2, which is comparable to 4U 1907 + 09 can be found at www.iras.ualgary.ca/~leahy/

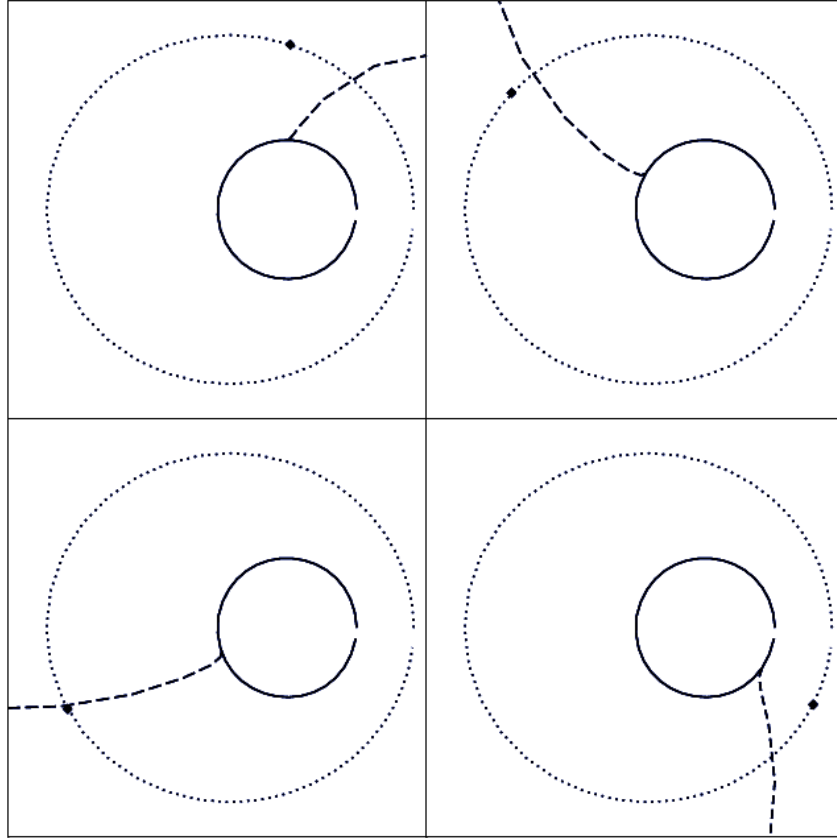


Figure 2: Binary geometry including the mid-line of the stream (dashed line) and neutron star (filled circle) on its orbit (dotted line) around the companion star (open circle) at four orbital phases: 0.15 (top-left), 0.35 (top-right), 0.6 (bottom-left) and 0.95 (bottom-right) (Kostka & Leahy, 2010).

strong magnetic fields arise from the progenitor. In most cases the magnetic field of solitary neutron stars will not or only slowly decay, due to the lack of external influences. But in binary systems, like 4U 1907 + 09, it is suggested that a long lasting and strong accretion can heat up the surface of the neutron star decreasing the conductivity, which causes a decrease in the strength of the magnetic field. It is also possible that a spin down due to accretion can cause a weakening of the magnetic field.

The magnetic field is assumed to have a dipole geometry and even though it decreases with r^{-3} , where r is the distance from the neutron star, it has a great influence on its vicinity. The magnetic field provides a pressure, which opposes the ram pressure from the infalling plasma. The distance from the neutron star, at which both are equal is the so called Alfvén radius or magnetospheric radius r_m (Eq. 1).

$$r_m = \left(\frac{\mu^4}{8 \cdot GM \cdot \dot{M}^2} \right)^{1/7} \quad (1)$$

It expands with an increasingly magnetic moment μ and a decreasing accretion rate \dot{M} and neutron star mass M . At the Alfvén radius the infalling plasma is forced to follow the magnetic field lines, no matter where it originates (from a disk, stellar wind or gas stream). But this can only take place, if the Alfvén radius is smaller than the co-rotation radius r_{co} , which is the distance from the neutron star at which Keplerian velocity equals the angular velocity of the magnetosphere and accordingly the angular

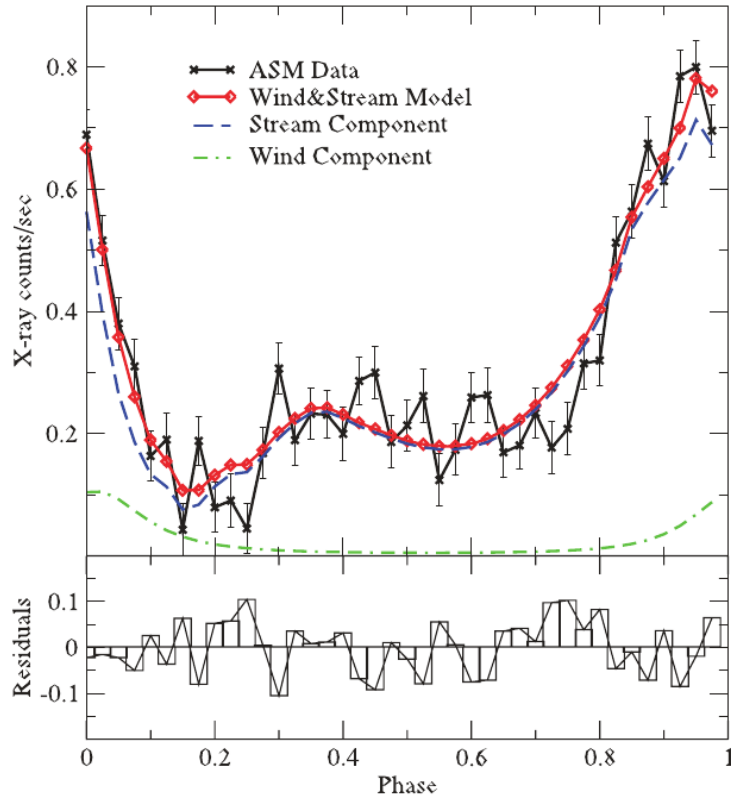


Figure 3: Model fit to the RXTE/ASM light curve (Kostka & Leahy, 2010).

velocity of the neutron star, as they form a solid rotator. The faster the rotation period of the neutron star the smaller is the co-rotation radius. In the other case the material had to move faster than the Keplerian velocity and therefore would not be able to be accreted leading to the switch-off of the X-ray emission. In the situation of almost equal radii $r_{\text{co}} \approx r_{\text{m}}$ variations in the \dot{M} can cause the X-ray emission getting switched on and off. If the Alfvén radius is much greater than the co-rotation radius this centrifugal barrier even causes the plasma to be expelled, which is the so called propeller effect. Figure 4 shows the geometry of such a system for the case of the accretion from an accretion disk. The transition region, in which the material is forced to move along the magnetic field lines is known as the boundary layer. Here there Alfvén radius describes also the inner edge of the accretion disk.

The trajectory of the material following the magnetic field lines will end up abruptly on the surface of the neutron star, where the magnetic field lines submerge (the magnetic poles). The material is stopped by Coulomb forces and deposit forming the polar caps. A hollow cylindrical geometry of the accretion column (Fig. 5 right) is more likely than the simple assumption of a solid accretion column (Fig. 5 left). The hollow cylinder is due to the coupling of the infalling plasma to magnetic field lines of a specific strength, leaving no material, which could couple to stronger lines closer to the neutron star. For weaker magnetic fields there is just no coupling. As the magnetic field is assumed to be a symmetric dipole the material will hit the surface in a narrow circular region around the pole.

In contrast to the geometry of the accretion column, the deceleration process is dependent on the accretion rate \dot{M} . A high accretion rate will cause the formation of a shock front above the point of impact, whose height depends on \dot{M} and can reach several neutron

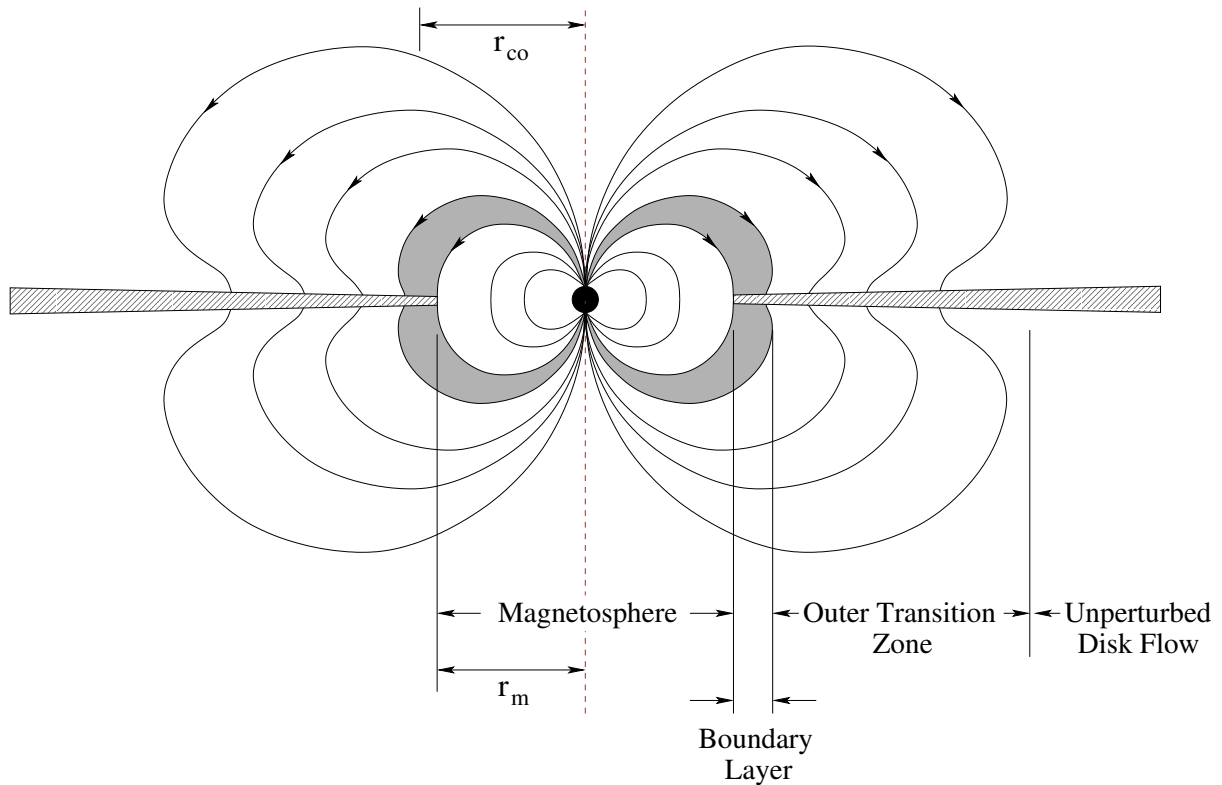


Figure 4: Geometry of a strongly magnetized neutron star (black circle) accreting from an accretion disk (shaded area), which is disrupted in the boundary layer (solid gray area). The plasma then follows the magnetic field lines (Kuster, 2004).

star radii. It is caused by the interaction of emitted photons with the very dense plasma decelerating the infalling supersonic plasma to subsonic speeds heating up the plasma. The so heated plasma emits X-ray photons, which only can escape perpendicular to the accretion column, describing a broad, fan beam like emission geometry (Fig. 6 left) as the accretion column is opaque. On the other hand, if \dot{M} is not high enough to form a shock front, i.e. the density in the accretion column is too low, the plasma will be stopped not until it reaches the surface, where X-ray photons will be produced by thermal bremsstrahlung and Compton cooling, which is radiated parallel to the column in a narrow pencil beam (Fig. 6 right; see also Becker & Wolff (2005)).

Considering an offset of the magnetic axis relative to the rotational axis, the thereby performed precession causes the X-ray emission region, the accretion column and mound at the poles, crossing the line of sight periodically. As that region emits in a broad angle a double peaked pulse profile can be seen on almost every viewing angle, since both poles occur during one rotation (also known as the lighthouse effect).

Another major aspect, which comes along with accretion, was not addressed so far, the transfer of angular momentum from the accreted material onto the neutron star. As almost all the accreted material has some angular momentum, independent where it originates, be it from stellar wind, accretion stream or disk. This transfer leads to changes in the rotation period and accordingly in the pulse period, which is observable in the X-ray band.

Since the theories about the mechanisms causing these period changes are rather complex, not well understood, and depend on the accretion process, only a brief

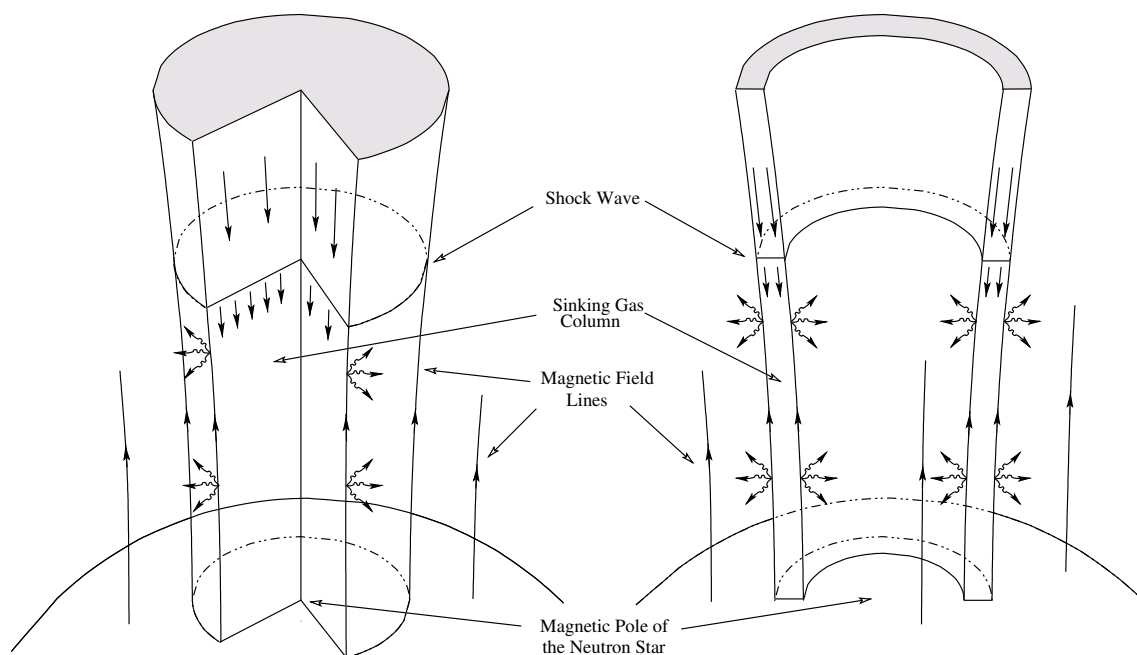


Figure 5: Accretion column above the magnetic poles a highly magnetized neutron star. A simple solid cylindrical column model on the left, on the right a hollow cylindrical accretion column, in which the width of the wall is small related to its diameter (Kuster, 2004).

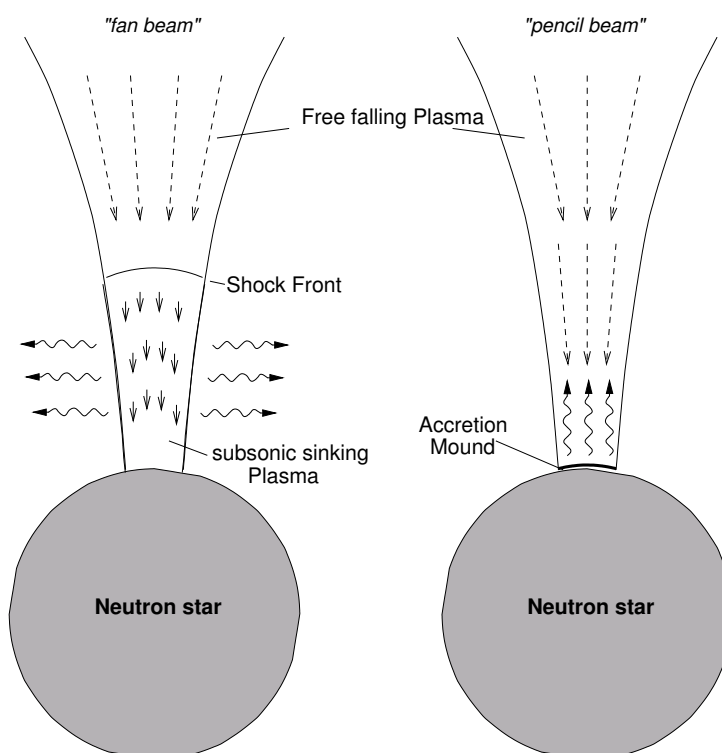


Figure 6: Schematic of the deceleration and radiation process depending on the accretion rate \dot{M} . (Kretschmar, 1996).

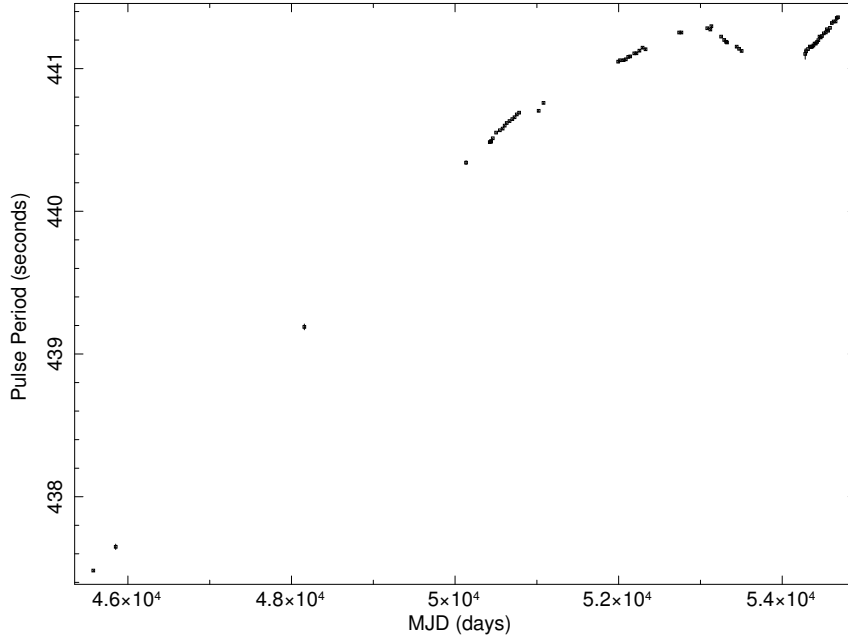


Figure 7: History of the pulse period measurements. For a detailed list of data see appendix 4. Figure from Inam et al. (2009).

overview will be given for a few of them and only those, which are applicable for 4U 1907 + 09. Figure 7 shows the history of the pulse period for 4U 1907 + 09 between August 1983 and August 2008. Until the end of 1997 4U 1907 + 09 had a steady spin down rate of $\dot{P}_{\text{Pulse}} = +0.230 \text{ s yr}^{-1}$, which then got cut in half and ended in a turnover in 2003. After that first torque reversal a short epoch of spinning up with a rate of $\dot{P}_{\text{Pulse}} = -0.158 \text{ s yr}^{-1}$ lasting at least until mid of 2005 (Fritz et al., 2006). After a second torque reversal between mid 2005 and mid 2007, which was not observed directly, leading again to a spin down rate with a comparable value to that between 1983 and 1997 (Inam et al., 2009). Also remarkable is that the X-ray luminosity of 4U 1907 + 09 has not changed significantly especially during the two torque reversals.

But what is the mechanism behind this behavior ?

The traditional model (Ghosh & Lamb (1979) and references therein) is based on a system, like it is shown in Figure 4, where the net torque transferred from a prograde accretion disk onto the neutron star is given by

$$N = n(\omega_s)\dot{M}\sqrt{GMr_0} \quad (2)$$

where M is the mass of the neutron star, r_0 the distance to the outer edge of the boundary layer, ω_s the so called fastness parameter defined by the ratio of angular velocity of the neutron star and the Keplerian velocity at r_0 . The dimensionless torque $n(\omega_s)$ is mainly dependent on the fastness parameter, which is expected to be small ($\omega_s \ll 1$) for slow rotators like 4U 1907 + 09. Therefore $n(\omega_s)$ is positive (see Fig. 3 in Ghosh & Lamb (1979)) and nearly constant for a large range of \dot{M} (see Fig. 5 in Ghosh & Lamb (1979)). A drastic decrease in \dot{M} may could cause $n(\omega_s)$ to become negative, but also a drop of the X-ray flux and additionally would imply a much smaller distance to 4U 1907 + 09 of the order of magnitude of 0.5 kpc, which was ruled out by the measurements of the stellar companion (Cox et al., 2005). Otherwise a significant growth of the magnetosphere may would lead to negative torques, which is also very unlikely to happen. Hence this

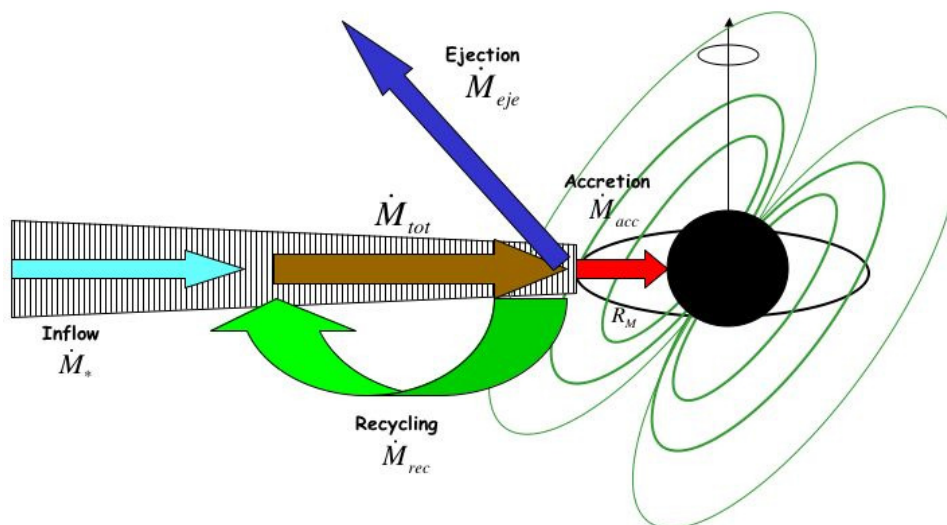


Figure 8: Accretion model provided by Perna et al. (2006), where \dot{M}_* is the mass inflow rate provided by the companion star, and \dot{M}_{acc} , \dot{M}_{rec} and \dot{M}_{eje} are, respectively, the accretion, recycling and ejection rate.

simple model would imply 4U 1907 + 09, as a slow rotator, to mainly spin up or to show luminosity dips during the torque reversals, which disagrees with the observations.

Furthermore in 't Zand et al. (1998) estimated the magnetospheric radius to be $r_m \sim 4300$ km and a co-rotation radius of $r_{co} \sim 12000$ km. Those values are also in contrary to the model above, as it assume the system to be near equilibrium ($r_m \sim r_{co}$) and moving out r_m would require a magnetic field of the order of 10^{14} G. Nevertheless in 't Zand et al. (1998) take the existence of quasi-periodic oscillations occurring in their observations as a strong evidence for the presence of an accretion disk with a small inner disk radius. And assuming that disk to be retrograde and transient with an duty cycle of a few percent could explain the long-term spin down rate. This torquing, however, would come along with an strong increase in the X-ray luminosity. But it is still difficult to explain the torque reversals of 4U 1907 + 09, as the different spin up and down rates would correspond to different duty cycles becoming noticeable in a change of the X-ray flux contradicting the observations.

As seen there is a need for a model, which reconciles the torque reversals without the need of changes in the X-ray flux. Such a model is provided by Perna et al. (2006). They suggest a more realistic scenario in the manner that they consider the magnetic field to be off axis by an angle χ with respect to the rotation axis. The further assumption of an equatorial prograde accretion disk makes it possible that the propeller effect is locally at work in one part of the disk, while in the other part material still gets accreted. This is due to the dependency of the magnetic field strength of the azimuthal angle leading to an asymmetric magnetosphere, i.e. that there are regions on a ring on the disk where $r_m \lesssim r_{co}$ is fulfilled as well as regions with $r_m \gtrsim r_{co}$. Additionally only a fraction of the expelled material possess enough energy to leave the system, the other fraction has not

and falls back onto the disk getting recycled (Fig. 8).

Therefore the recycling of material can cause variations in the rate of accretion without any changes in the inflow rate provided by the companion. Furthermore the authors pointed out that in the case of $\chi > \chi_{\text{crit}}$, where χ_{crit} is between 25° and 45° , “*periodic variations between spin-up and spin-down states take place without requiring the presence of any external, periodic, and fine-tuned perturbation*”. This model would reconcile the observed pulse period history of 4U 1907 + 09 with its two torque reversals within a short time, if there was not the prediction of the model that torque reversals are a rare events. But as it is stated this model is very simplified as it does not account variations of \dot{M} , which can occur e.g. due to an eccentric orbit, like in 4U 1907 + 09, or other sources of torque, such as magnetic stress, like Ghosh & Lamb (1979) did in their model. Also a more realistic accretion disk, which are warping and precessing, should be assumed.

In the end there is no totally satisfying model, which could explain the evolution of the pulse period. Beyond that all mentioned models relying strictly on the existence of an accretion disk, but according to the conclusions of Kostka & Leahy (2010) that the measurements of Rivers et al. (2010) rule out the presence of an accretion disk in 4U 1907 + 09 all of these are scotched. Although their wind and stream accretion model can nicely reconcile the double humped orbital light curve they still have to provide an explanation for the pulse period evolution or it has to be shown, that it is consistent with the existence of an accretion disk. All this requires further investigations.

2 The Rossi X-ray Timing Explorer (RXTE)

As the aim is to estimate the trend of the pulse period of 4U 1907 + 09 X-ray measurements are needed, but as such radiation is not able to reach the Earth the observations can only be accomplished properly by instruments like balloons, rockets, and satellites, in the upper layers of the atmosphere. Furthermore the imaging of X-rays is not as easy as in the optical band, because there is no material with a large enough angle of total reflection for X-rays. The 1995 launched Rossi X-ray Timing Explorer (RXTE) is based on the collimator technique to measure X-ray radiation, which is the simplest method besides the coded mask and the nested paraboloidal/hyperboloidal reflectors used by e.g., *INTEGRAL* and *XMM-Newton*, respectively. The basic composition of a collimator is simple: on top of a detector there are a bunch of tubes consisting of absorbing material limiting the field of view.

RXTE (Fig. 9) harbors three different detectors, namely the proportional counter array (PCA), the high energy X-ray timing experiment (HEXTE) and the all sky monitor (ASM). The PCA, which is used in this thesis exclusively, consists of five identical coaligned Xenon proportional counter units (PCUs; Fig. 10) with a field of view of 1 degree and nominally covers an energy range from 2 to 60 keV (or rather 2 to 100 keV due to voltage changes to improve detectors lifetime). But as the effective area of the PCA drops down from $\sim 6000 \text{ cm}^2$ between 6 keV and 10 keV to less than 1 cm^2 at 34.6 keV, due to the Xenon edge, the recommended energy range is between 2 keV to $\sim 60 \text{ keV}$. (Fritz (2008), Kreykenbohm (2004))

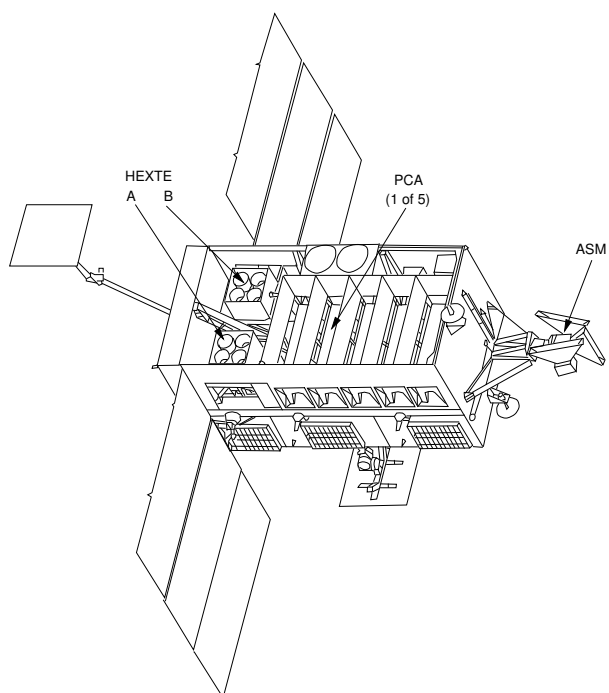


Figure 9: Schematic of RXTE spacecraft with its two HEXTE clusters at the right, the PCA consisting of five coaligned PCUs in the middle and All Sky Monitor (ASM) attached outside. Figure from (Wilms, 1998).

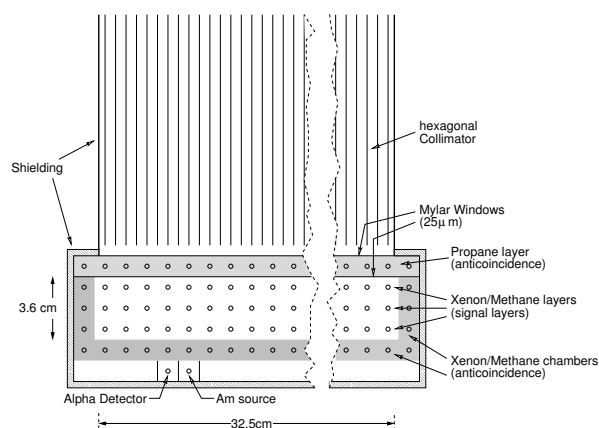


Figure 10: Schematic of one of five Proportional Counter Unit (PCU) arranged in the Proportional Counter Array (PCA) . Figure from Wilms (1998).

The spacecraft itself is on a low earth orbit (LEO) with an orbital period of 90 minutes. The orbital altitude is small enough to go below the radiation and particle belts around the earth (*van Allen belts*). Therefore *RXTE* is mainly protected against their influences. Only in the region of the South Atlantic Anomaly (SAA), where a dent in the earth's magnetic field let particle penetrate closer to the ground, *RXTE* is endangered (detail studies of the SAA see Fürst et al. (2009)). While passing this region the instruments on board are shut off to prevent them being damaged.

3 Observation and data reduction

The data, which will be analyzed in this work, are provided by the High Energy Astrophysics Science Archive Research Center (HEASARC). The intention is to continue the investigations of the evolution of the pulse period exhibited by 4U 1907 + 09 using a method which was also used by Inam et al. (2009). The observations cover an epoch from June 2007 (ObsID: 93036-01-01-00) until July 2010 (ObsID: 95350-01-14-00). The data until August 2008 (ObsID: 93036-01-30-00) were already evaluated by Inam et al. (2009).³ Nevertheless these data were also included, as they provide the possibility to verify the correctness of the analysis method, which will be discussed below. An overview of all observations is given in Table 5 in the appendix. They span a total exposure time of 128 ks, in which each observation is between 0.73 ks and 2.76 ks long. In the first step the data got extracted out of the raw data⁴, in which the energy channels 0-4 are excluded as they cause conflicts with the GoodXenon extraction modus. Therefore energy channels 5 corresponding to 1.95 keV (PCU0) and 2.06 keV (PCU1-4) up to channel 255 corresponding to 126.87 keV (PCU0) and 117.86 keV (PCU1-4) were extracted, although the accuracy of the higher energy channels is not very good, but as only the lightcurves are of interest this does not matter.⁵ The time resolution was set to 1 s even though this is comparatively high with respect to the achievable resolution of 1 μ s, but as the expected pulse period is in the order of 441 s it is sufficient and a smaller resolution would also need much more storage and therefore more calculation time and would have a worse signal to noise ratio.

Table 1: Binary orbit of 4U 1907 + 09

Parameter	Symbol	Value
Orbital period	P_{orb}	8.3753(1) days
Eccentricity	e	0.28(4)
Orbital epoch	$T_{\pi/2}$	MJD 50134.76(6)
Longitude of periastron	ω	330(7) $^\circ$
Projected semi-major axis length	$a_x \sin i/c$	83(2) lt-s

Additionally a barycentric correction was directly applied during the extraction. Because of the orbit of *RXTE* around the Earth and the Earth's motion around the sun the precise measured time has to be corrected for the light-travel difference, which are at maximum 16 minutes (for a time difference of a half year), and also for the Doppler effect. As this trajectory is well known it can be corrected for. Of course this effect also occurs for the orbital motion of 4U 1907 + 09. This binary correction was applied using the values provided by in 't Zand et al. (1998) and listed in Table 1.

After having extracted the data, of which the lightcurve for every observation can be seen in Figure 24 in the appendix, the electron excess ratio occurring during each observation was checked. There was no significant exceed of the recommend 0.1 threshold and

³The ObsIDs format is given by NNNNN-*TT*-*VV*-*SS*, where NNNNN is the proposal number, *TT* is the target number, *VV* is the viewing number tracking the number of scheduled looks, and *SS* is the sequence number identifying different pointings included in one viewing, which are all assigned by the Guest Observer Facility (GOV).

⁴Raw data in the sense as they are provided by HEASARC.

⁵Values according to http://heasarc.gsfc.nasa.gov/docs/xte/e-c_table.html

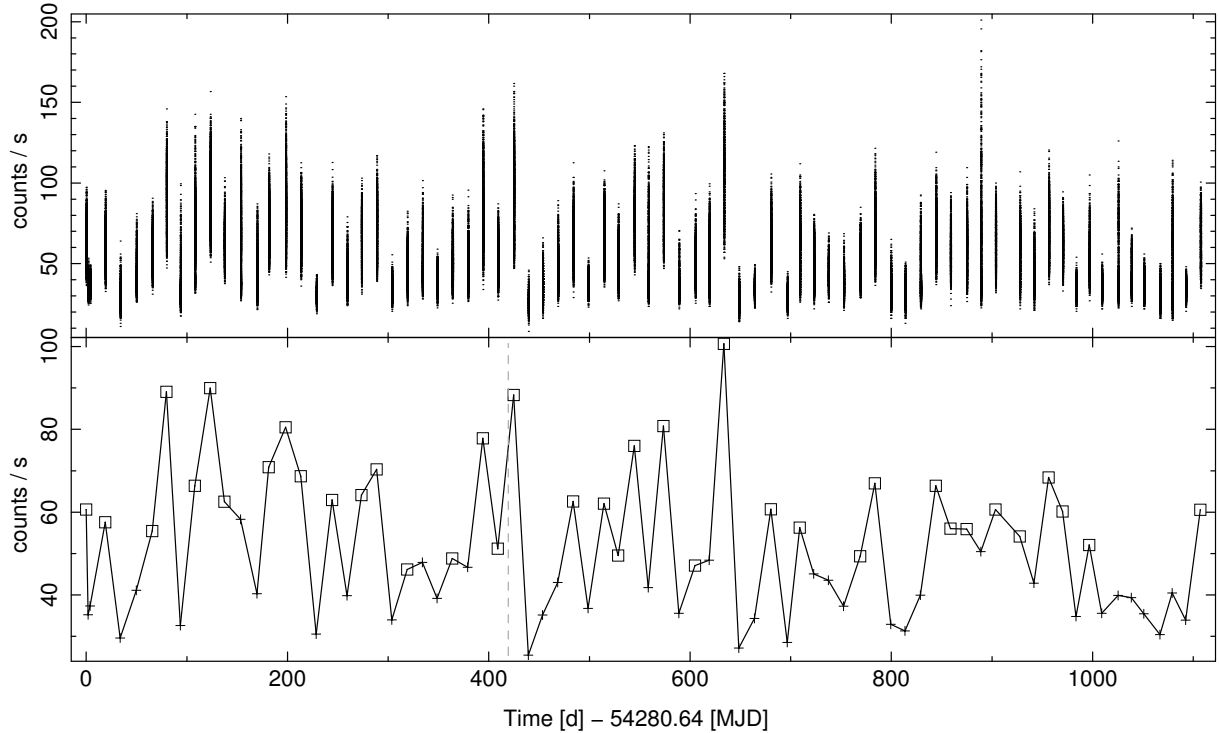


Figure 11: Top: Combination of all lightcurves. Bottom: Combination of the mean luminosity of every observation. Squares mark observations, which show a well defined peak in the epoch fold, crosses mark the rest. Data until the vertical dashed gray line were already evaluated by Inam et al. (2009). Both graphs are normalized respectively the number of PCUs.

therefore no data had to be sorted out due to electron noise, which monitors possible contaminations of the data with unintentional events.

A combination of all lightcurves is shown in Figure 11. The top graph is the simple sequence of all observations, while in the bottom graph for clarity the mean luminosity of every observation is shown. Note that every lightcurve was normalized to the number of PCUs, which were active during the measurement.

It is obvious, that not all lightcurves (see appendix Fig. 24) are suited for the pulse period estimation, as many do not show any periodic pulsation of the requested timescale. Therefore another selection, besides the electron excess ratio, was applied as it is described in the following.

For all lightcurves an epoch folding with a fold period between 380 s and 500 s was carried out. Simple spoken the epoch fold technique cuts the given lightcurve into intervals with a length of the chosen fold period and sums them up. The output is the deviation (χ^2) from a linear fit. The larger that output value is, the more probably is it that the related fold period is the real pulse period. For more information on the epoch fold method see Schwarzenberg-Czerny (1989), Leahy et al. (1983), Larsson (1996) and Davies (1990). Those lightcurves, whose epoch fold possess a well defined peak around the expected pulse period were taken into account for further calculations. This selection was achieved by setting a threshold of 600 for the χ^2 value of the epoch fold. This value was adjusted manually by looking through all epoch folds and lowering the threshold to a value, which would include all data with a well defined peak (see Fig. 12). As it is shown in Figure 11 the selected data (squares) are mostly during bright phases

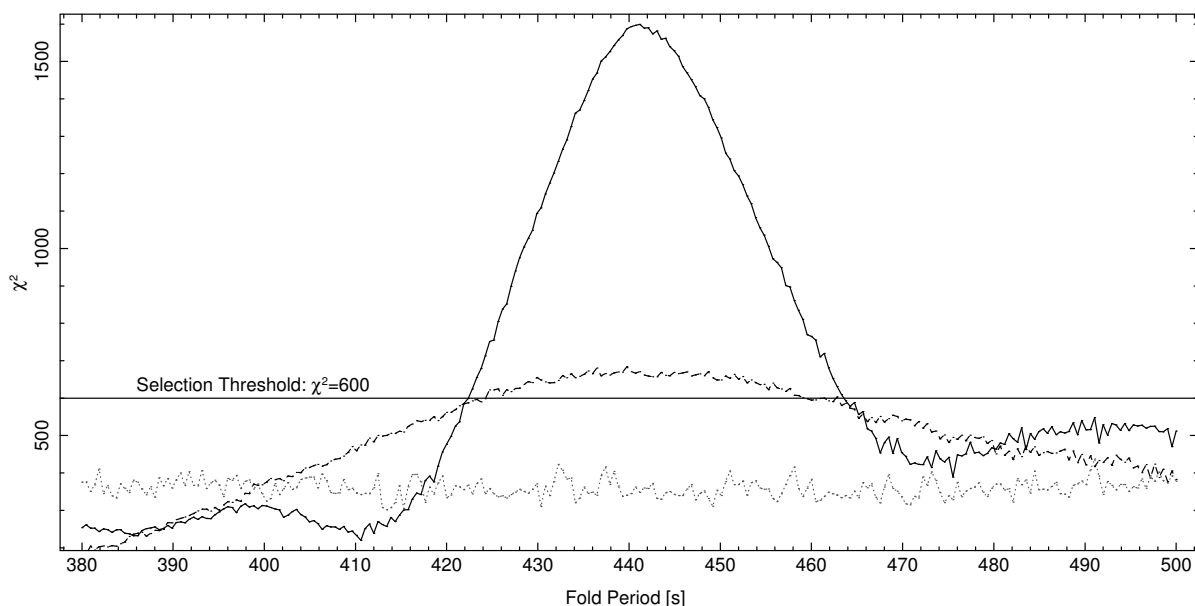


Figure 12: Epoch fold and data selection example. Solid line corresponds to observation #5, dashed line to observation #36 and dotted line to ObsID: 94036-01-08-00.

of 4U 1907 + 09, but also some data of less bright phases were selected, which would be sorted out by a luminosity threshold even if those also exhibit a sufficient pulse period. In Table 2 the selected observations, now spanning an exposure time of 64 ksec, are listed with assigned observation numbers, which will be used for further references and additionally in Figure 13 the epoch folds of these data are shown in a color-coded map. On closer examination of Figure 13 it is obvious that a simply epoch fold is not able to provide an acceptable pulse period as the peak is very broad and therefore it is afflicted with a huge error in the order of magnitude of several seconds. The reason for this issue is the short duration of each observation as they only include between 1.7 and 6.3 pulses. But an improvement by combining observations is questionable as well due to the mean separation of two weeks between each observation and a predicted change of almost 0.01 s in the pulse period during this time. Nevertheless an attempt was carried out combining two adjacent observations ([1,2], [2,3], ...).⁶ Contrary to the expectations this attempt resulted in even worse epoch folds. Hence the observations were treated individually.

Further it is notable that Inam et al. (2009) had the advantage of having 3 observations within a week (see Tab. 5 first 3 observations), which they could use to achieve a good pulse period. This is not the case for the new data set. Anyhow the duration and separation of the observations were chosen, founded on the pulse period history of 4U 1907 + 09, such that the determination of the pulse period evolution should be possible with the method explained in the next section.

⁶That kind of observation combination was probably used by Inam et al. (2009) for their evaluations, but this was recognized lately so it was not applied in this thesis.

Table 2: Observations meeting the selection criteria (see text).

#	ObsID	Date [DD.MM.YYYY]	[MJD]	Duration [ks]	#PCU
0	93036-01-01-00	29.06.2007	54280.6	1.90	3
1	93036-01-04-00	18.07.2007	54299.6	1.76	3
2	93036-01-07-00	03.09.2007	54346.2	2.06	2
3	93036-01-08-00	17.09.2007	54360.4	1.55	3
4	93036-01-10-00	15.10.2007	54388.5	1.77	3
5	93036-01-11-00	30.10.2007	54403.9	2.76	3
6	93036-01-12-00	13.11.2007	54418.0	1.79	3
7	93036-01-15-00	28.12.2007	54462.1	1.66	3
8	93036-01-16-00	13.01.2008	54478.7	2.00	2
9	93036-01-17-00	28.01.2008	54493.8	1.42	2
10	93036-01-19-00	28.02.2008	54525.0	1.65	3
11	93036-01-21-00	29.03.2008	54554.0	1.20	2
12	93036-01-22-00	13.04.2008	54569.1	1.36	2
13	93036-01-24-00	13.05.2008	54599.5	1.84	2
14	93036-01-27-00	27.06.2008	54644.4	2.35	2
15	93036-01-29-00	27.07.2008	54674.6	1.57	2
16	93036-01-30-00	11.08.2008	54689.5	1.88	2
17	93036-01-31-00	27.08.2008	54705.4	1.77	3
18	93036-01-35-00	25.10.2008	54764.4	1.54	2
19	93036-01-37-00	25.11.2008	54795.1	1.95	2
20	93036-01-38-00	09.12.2008	54809.2	2.23	2
21	93036-01-39-00	25.12.2008	54825.1	1.66	2
22	94036-01-02-00	23.01.2009	54854.2	1.37	2
23	94036-01-04-00	23.02.2009	54885.7	1.90	2
24	94036-01-06-00	24.03.2009	54914.3	0.94	1
25	94036-01-09-00	09.05.2009	54961.0	1.50	2
26	94036-01-11-00	07.06.2009	54989.5	1.80	1
27	94036-01-15-00	06.08.2009	55049.5	1.64	2
28	94036-01-16-00	21.08.2009	55064.3	1.81	2
29	94036-01-20-00	20.10.2009	55124.7	1.13	2
30	94036-01-21-00	04.11.2009	55139.3	1.61	2
31	94036-01-22-00	20.11.2009	55155.4	1.39	2
32	94036-01-24-00	19.12.2009	55184.1	1.92	2
33	95350-01-01-00	12.01.2010	55208.2	1.95	1
34	95350-01-03-00	09.02.2010	55237.0	1.84	2
35	95350-01-04-00	23.02.2010	55250.7	1.92	2
36	95350-01-06-00	22.03.2010	55277.3	1.12	2
37	95350-01-14-00	10.07.2010	55387.8	0.86	2

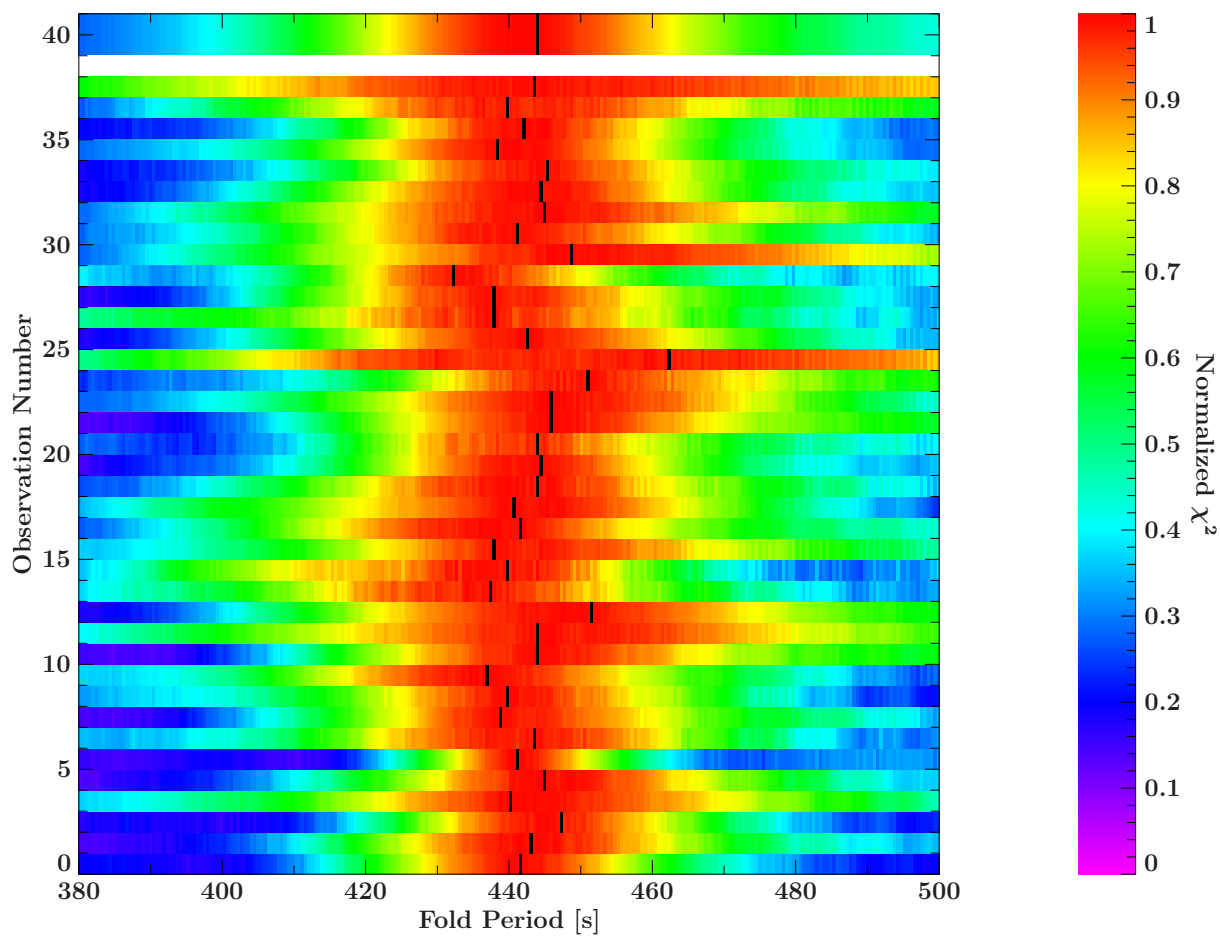


Figure 13: Epoch folds of selected data presented in a color-coded map. The maximum of each epoch fold is marked with a black bar. The chi square of the epoch fold output was normalized respectively each maximum. In the top two panels above the white panel show the sum of all epoch folds below (panel 0-37).

4 Data analysis

As it was shown in the last section a simple epoch fold of a single observation or a combination of observations is not useful. Therefore another method is required, which is able to deal with the given data. The trick is not to measure each single pulse period, but phase differences of the pulse profiles with respect to a fixed reference pulse profile.

4.1 Phase connection

The idea behind the phase connection is as follows. First consider a lightcurve with a constant ($\dot{P} = 0$) periodical peak represented by a dash-dotted line in Figure 14. Additionally consider a signal with the same period, but which changes with time ($\dot{P} \neq 0$) illustrated by the dotted plus solid line with $\dot{P} = +0.015$ (top) and $\dot{P} = -0.015$ (bottom) per period, while the first shown peak is taken as reference point. The further away from the reference point the larger is the gap between the peak of the constant signal and the corresponding \dot{P} afflicted peak (in this case it is increasing quadratically) and therefore it is more useful to set the reference point to a peak in the middle. The trick now is to determine the value of this gap, which allows to reconstruct the non-constant signal without knowing about the value of \dot{P} .

Applying this basic idea to real observations, the first step is to choose one observation out of the set, preferably in the middle of the covered epoch. For this observation, however, an accurate pulse period is needed, which is used for a period fold for all observations. A period fold simply cuts a lightcurve into pieces, whose length is the given period and sums them up. In this way a pulse profile is created. Folding all observation onto the same period P_{ref} and onto the same reference time t_0 , which is normally the point of time at which the reference observation started, leads to pulse profiles with different phase offset $\Delta\Phi$. To a certain extent $\Delta\Phi$ coincides with the gap described above and therefore needs to be determined accurately, which can be achieved for example with an one dimensional cross correlation, which was also used in this work. But this comparison or any other method of course can only provide values in an interval of the length of only one pulse, but the wanted gap can exceed this length.

This issue is also illustrated in Figure 14, in which peak I or accordingly pulse I overlaps with the given constant signal per definition. Peak II, however, already visibly deviates from the main period, but an attribution to the corresponding reference peak is still possible even if only phase [4,5] is observed. In contrast peak III drifted into the next/previous phase interval and therefore an exact attribution is not possible without knowing how many pulses had elapsed.

Nevertheless it is possible to correct for this miscounting by manually adding or subtracting an integer to $\Delta\Phi$. The question whether adding or subtracting depends on the way $\Delta\Phi$ is counted. The most intuitive method for further calculations would be to define $\Delta\Phi$ as the smallest difference between the phase position of the peak of the constant pulse signal and the peak of the \dot{P} afflicted pulse. This definition permits to differentiate between the case of $\dot{P} < 0$ for $\Delta\Phi > 0$ and $\dot{P} > 0$ for $\Delta\Phi < 0$, if and only if there is no miscount for the first observed peak. The only other alternative to differentiate between $\dot{P} < 0$ and $\dot{P} > 0$ necessitates two sufficient accurate pulse periods or to get this information from former measurements and the sureness there is no change of sign in \dot{P} afterwards. In the first place it is only relevant to obtain proper $\Delta\Phi$ s regardless how it is defined exactly. In this work $\Delta\Phi \in [0,1]$ as this is the natural output range of the

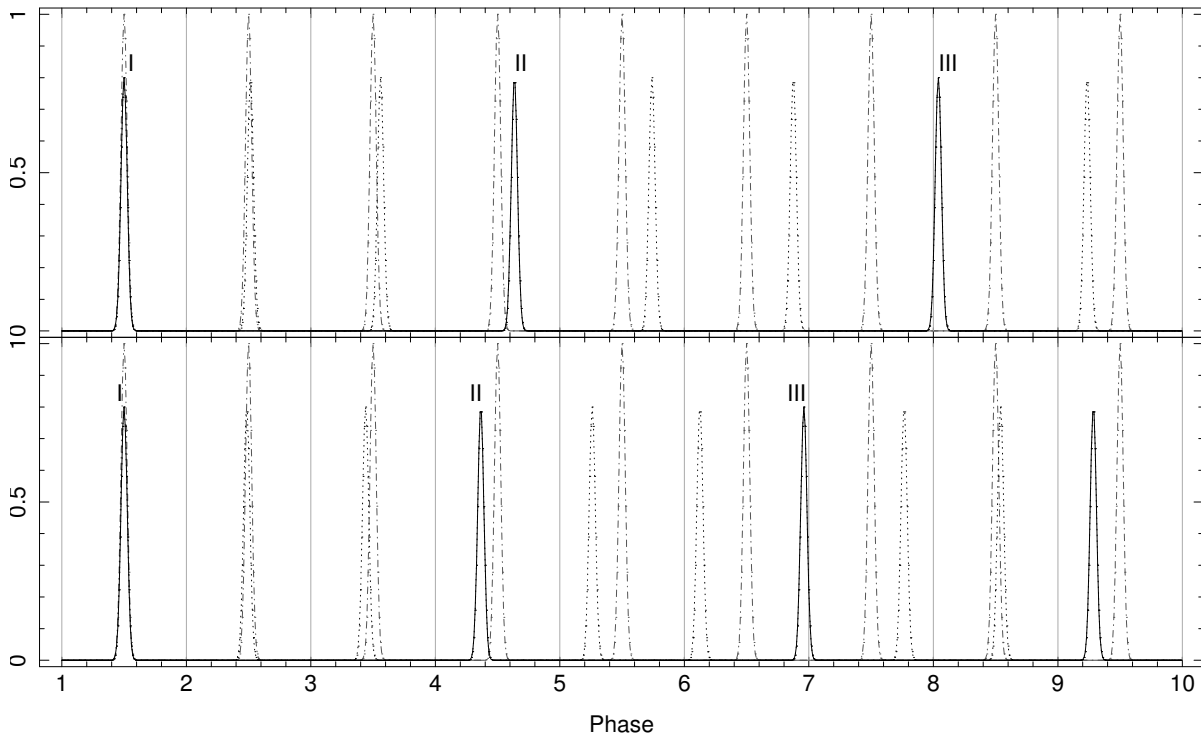


Figure 14: Illustration of the theoretical background of the phase connection analysis method. The dash-dotted line represents a periodical pulse with a period of one chosen observation, which acts as reference period P_{ref} , and $\dot{P} = 0$. The x-axis is normalized to this pulse period. The dotted line with a smaller amplitude has the same period, but additionally change in period of $+0.015$ with each pulse in the top graph and -0.015 in the bottom one. Black solid lines mark observed pulses.

maximum of the one dimensional cross correlation of the two pulse profiles, whose x-axes are normalized to the reference pulse period. As long as $\Delta\Phi \in [0, 0.5[$ for the first phase shift is fulfilled, which corresponds to $\dot{P} > 0$, as it is implied by the results of Inam et al. (2009) (see also Fig. 7) there is no difference to the method above.

But to do a proper phase correction a model is needed, which describes the time dependent change of the period. It is common to use a polynomial function with degree two or three (Eq.3)

$$\delta\Phi(t) = \Phi_0 + \delta\nu(t - t_0) + \frac{1}{2}\dot{\nu}(t - t_0)^2 + \frac{1}{6}\ddot{\nu}(t - t_0)^3 \quad (3)$$

where $\delta\Phi$ is the corrected pulse phase offset, t_0 is the start-time of the observation, Φ_0 is the phase offset at t_0 , $\delta\nu$ is the deviation from the reference pulse frequency including the additive phase correction, $\dot{\nu}$ and $\ddot{\nu}$ are the first and second pulse frequency derivatives of the source. This formula is motivated by a Taylor expansion and includes an additional degree of freedom compared to the scenario stated above.

With this model it is possible to find the phase correction Φ_{cor} by fitting it to the estimated $\Delta\Phi$ s, which are primarily all within the interval $[0, 1[$. Starting at the reference point going outwards to each of those $\Delta\Phi$ s integer has to be added until the resulting Φ contribution fits the model best. A constructed simple example for this procedure is shown in Figure 15, in which the triangles represent the $\Delta\Phi$ s and the squares the phase corrected values $\delta\Phi$, while the gray horizontal lines show the correction value. Values

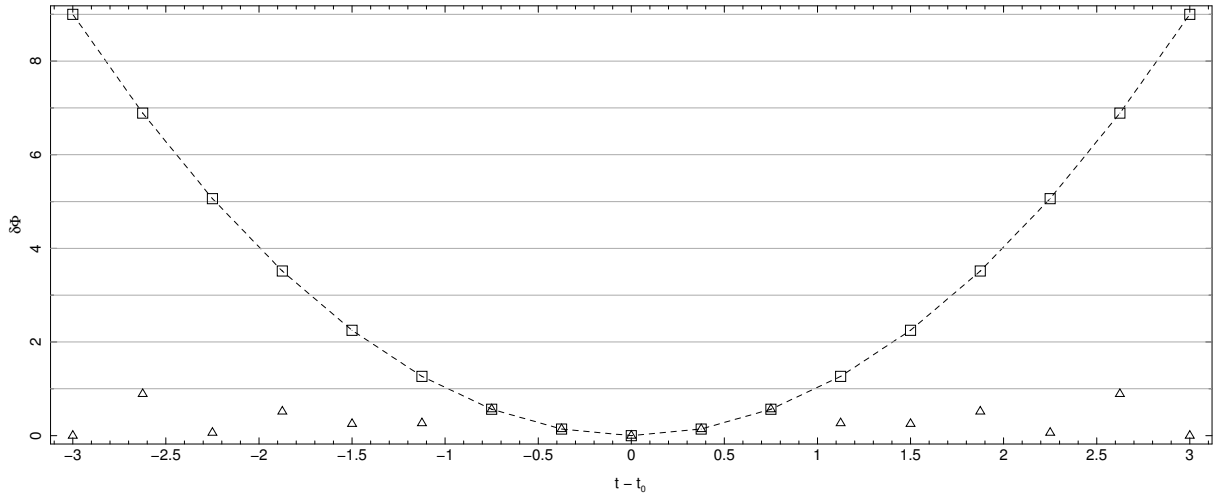


Figure 15: Constructed example for the phase correction procedure. Triangles represent the $\Delta\Phi$ s, squares the phase corrected values $\delta\Phi$ and gray horizontal lines show the correction value. The model fit is given by the dashed line.

close to the reference point at $t = t_0$ have not to be corrected. This proceeding of course is not exact, but there is no other way to do so yet.

Based on this formula $\nu(t)$ can be obtained by differentiation and adding the reference pulse frequency/period ($\nu_{\text{ref}} = 1/P_{\text{ref}}$) of the reference observation:

$$\begin{aligned} \nu(t) &= \nu_{\text{ref}} + \delta\nu + \dot{\nu}(t - t_0) + \frac{1}{2}\ddot{\nu}(t - t_0)^2 \\ P(t) &= \left[\nu_{\text{ref}} + \delta\nu + \dot{\nu}(t - t_0) + \frac{1}{2}\ddot{\nu}(t - t_0)^2 \right]^{-1} \end{aligned} \quad (4)$$

But this phase connection method associated with the assumed model has its limits and requirements:

1. Carrying out a period fold for all observations with the same period, although $\dot{P} \neq 0$ and $\ddot{P} \neq 0$ is not naturally as a period fold onto a wrong period causes poor pulse profiles, which prevent to get a proper value for $\Delta\Phi$. Therefore both values, \dot{P} and \ddot{P} , need to be sufficiently small or in other words the pulse profile must not significantly change. But as it is shown in Figure 13 all epoch folds are consistent with one fold period due to the width of the peaks, i.e. the sum of all epoch folds shows only one peak with a width comparable of each single epoch fold.
 2. The accuracy of the additive correction Φ_{cor} decreases rapidly with the distance to the reference point dependent on the magnitude of \dot{P} , i.e. the greater the correction the less accurate it is.
- ⇒ There is a limited time window in which this method is applicable. The determination of the exact dimension of this window is not trivial and would go beyond the scope of this work.
3. If \dot{P} changes with time to rapidly or there is even a change of sign in \dot{P} the determination of the right correction is almost impossible using only two observations, meaning all higher derivatives of P have to be sufficient small. Hence this method

is only expediently applicable for phases in which $\dot{P} \approx \text{const.}$ and especially no torque reversals can be modeled.

4. A good coverage with observations, especially close to the reference point, where no correction is needed, is beneficial as this constrains the parameter of the model.
5. A reliable determination of the reference period is a basic requirement, which is a problem in this work as the epoch folds show (Fig. 13) and will be discussed below.

A further major problem is to estimate a proper error in $\Delta\Phi$ and for the phase correction and therefore also in equation (3) and (4). To provide a statistical significant error is also beyond the scope of this work, but can be achieved with Monte Carlo simulations. Nevertheless an attempt to provide at least an error for the comparability among each values was done. As $\Delta\Phi$ is calculated by an one dimensional cross correlations of the reference pulse profile and a pulse profile of another observation, which were derived from period folds with a given binning, the output of the cross correlation underlies the same binning. The maximum of the cross correlation was taken to be $\Delta\Phi$ and therefore the probability is higher to pick the right bin the wider its width, which is given by $w_{\text{bin}} = 1/\#\text{bins}$. But an increase in the bin width also means a decrease in the accuracy. By manually looking through the cross correlations with different binning a hand made function was derived (first two factors in Eq.(5)), which seems to reconcile with those issues. This means that those two factors were constructed to describe an error which is for a low count of bins of the size of one bin, but the narrower the bins get the larger becomes their error. Also the correlation strength CS was taken into account, as this value indicates how likely it is that the compared pulse profiles are correlating and therefore give a hint if there is a major change in them. Per definition CS lies between -1 and 1, but for the chosen data its maximum typically has values within [0.6,1]. Eventually the error in $\Delta\Phi$ was calculated with the following function:

$$\Delta(\Delta\Phi) = \log(\#\text{bins} \cdot \log(\#\text{bins}))^2 \cdot \frac{\log(\#\text{bins})}{50 \cdot \#\text{bins}} \cdot \frac{1}{CS^4} \quad (5)$$

The errors of $\delta\Phi$, $\nu(t)$ and accordingly of $P(t)$ are calculated by error propagations including the fit parameters errors. But as they all include $\Delta(\Delta\Phi)$ these errors are not statistically significant!

Having discussed the analysis proceedings, it will now be applied to the observations given in Table 2. As this is close to what Inam et al. (2009) did and due to the lack of the possibility to obtain an accurate reference pulse period from that data, this method first is tested with the data set Inam et al. (2009) has used, too. The best approach for P_{ref} is to use equation (4) with the fitting parameters provided by Inam et al. (2009) (see Table 3). In Figure 16 only data were taken into account with observation numbers between 0 and 16, which were also used by Inam et al. (2009) and additionally the same reference point (obs. number 7) was chosen. In the left upper corner this configuration can also be seen, while the first number is the observation number of the used reference point and the interval shows, which data were included. From now on this nomenclature will be used. Only the three parameter $\delta\nu$, $\dot{\nu}$ and $\ddot{\nu}$ of Eq.(3) were used as free parameter for the model fit, while Φ_0 and t_0 were fixed to the values of the reference point. The top graph of Figure 16 shows the fitted model (solid line) to the corrected $\Delta\Phi$ s (squares),

Table 3: Fit parameters according the model in Eq.(3) provided by Inam et al. (2009). Thereby $\nu = \nu_{\text{ref}} + \delta\nu$.

Parameter		Value
Epoch	t_0	MJD 54467.6(1) Days
Spin Frequency	ν	$2.266460(2) \cdot 10^{-3}$ Hz
Spin Frequency Derivative	$\dot{\nu}$	$-3.59(2) \cdot 10^{-14}$ Hz s ⁻¹
	$\ddot{\nu}$	$-5.3(4) \cdot 10^{-22}$ Hz s ⁻²

while the circle marks the reference point. The middle graph shows the residuals, i.e. the difference between each data points and the fitted model. In the bottom graph the resulting periods according to equation (4) are shown (squares) together with the periods Inam et al. (2009) had estimated (triangles). The dash-dotted line is the period evolution calculated with the fit values shown in Table 3 together with the given errors (dotted lines). This test analysis shows the correctness of the procedure described above insofar that it reproduces the results of Inam et al. (2009) very good.

In the next Figure 17 all selected data were fitted. But now there is a big gap visible with respect to the predicted period evolution increasing with time. More precisely the estimated periods are not consistent with the prediction, as they do not overlap within their errors. But the needed phase corrections are very high and as stated above the higher this value is the more inaccurate is it and hence the periods, which arise from data afflicted with a high Φ_{cor} are not reliable. Therefore it is questionable if those periods are appropriate. Nevertheless the fitted model results in pulse periods, which are at least consistent with the pulse periods of Inam et al. (2009) until 54682 MJD.

An obvious solution would be to move the reference point to later observations. But by doing so the data were harder to fit to the model and were furthermore mostly inconsistent with the model of Inam et al. (2009) and their estimated periods even though the reference point was still within the Inam data set. Although a few budding fits were among them, they were discarded too, because using the same set of data and only moving the reference point should not result in different models! This situation got even worse with only accounting new data. This problem is most likely due to the way the reference period P_{ref} is calculated (using Eq. 4 and Inam model fit values from Table 3) as it is not sure, if the Inam model provides values for the pulse period, which are accurate enough. Furthermore the period evolution must not be as predicted as it is also indicated by the fitted model in Figure 17. And as the whole phase connection procedure relies on that value, even small deviations from the real value can cause totally wrong models. Additionally there are no proper indications that the used reference period is suitable, i.e. it is hard to recognize whether it is right or wrong. For great deviations, however, this can be checked by looking at the scatter of the $\Delta\Phi$ close to the reference point, which are too large if P_{ref} is wrong. For example this is the case if those values of $\Delta\Phi$ next to the reference point, which do not need a correction, on the left strongly deviates from the according ones on the right assuming equal distances from the reference point for each corresponding point. In Figure 18 some examples are shown for this issue.

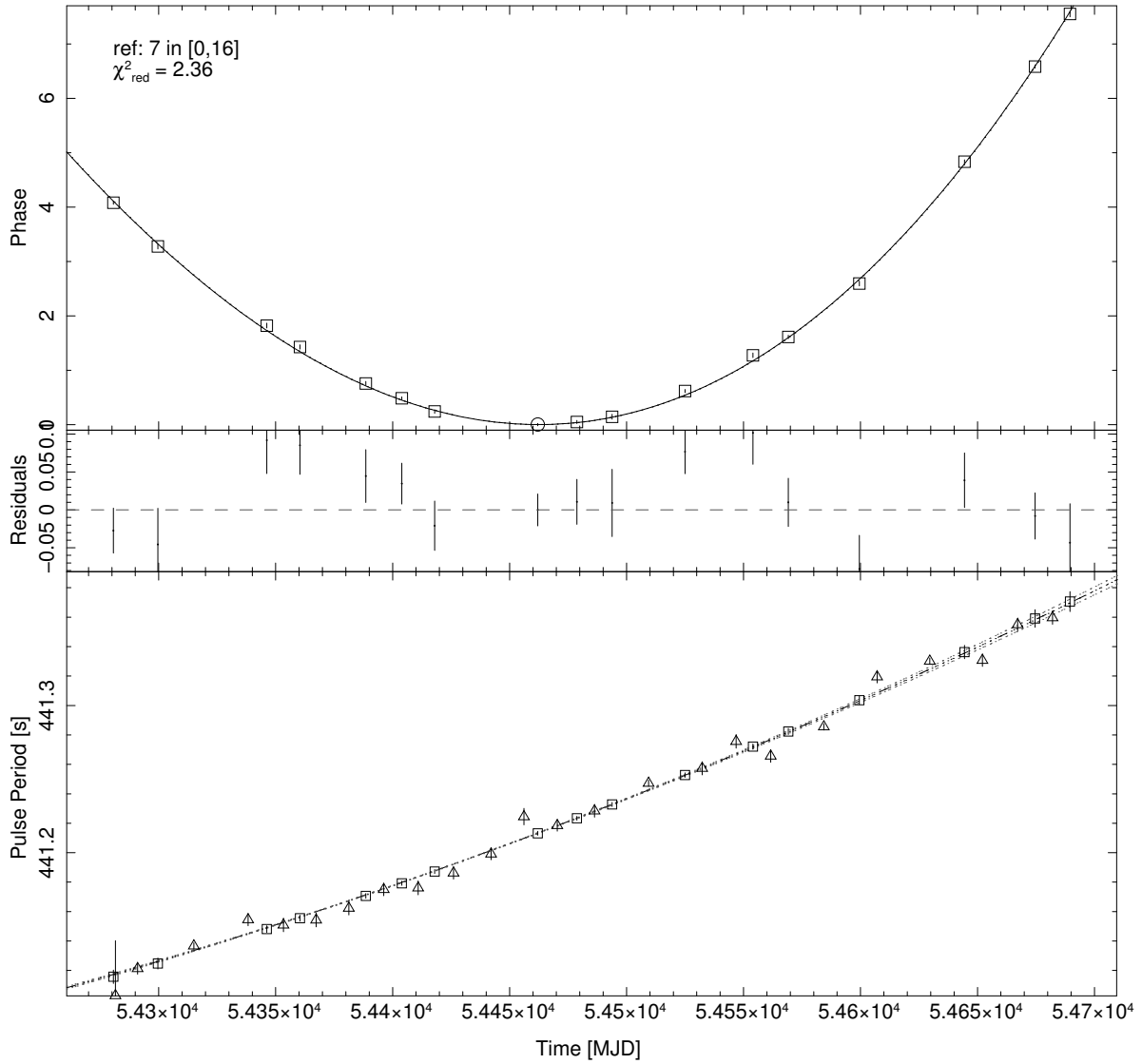


Figure 16: Model fit to the data configuration 7 in [0, 16]. Top: Model fit (solid line) to the corrected $\Delta\Phi$ s (squares), the circle marks the reference point. Bottom: Resulting periods (squares) together with the periods calculated by Inam et al. (2009) (triangles) and the period evolution according the parameters shown in Tab.3. Detailed list of all values and fit parameter see appendix Table 9 and 10.

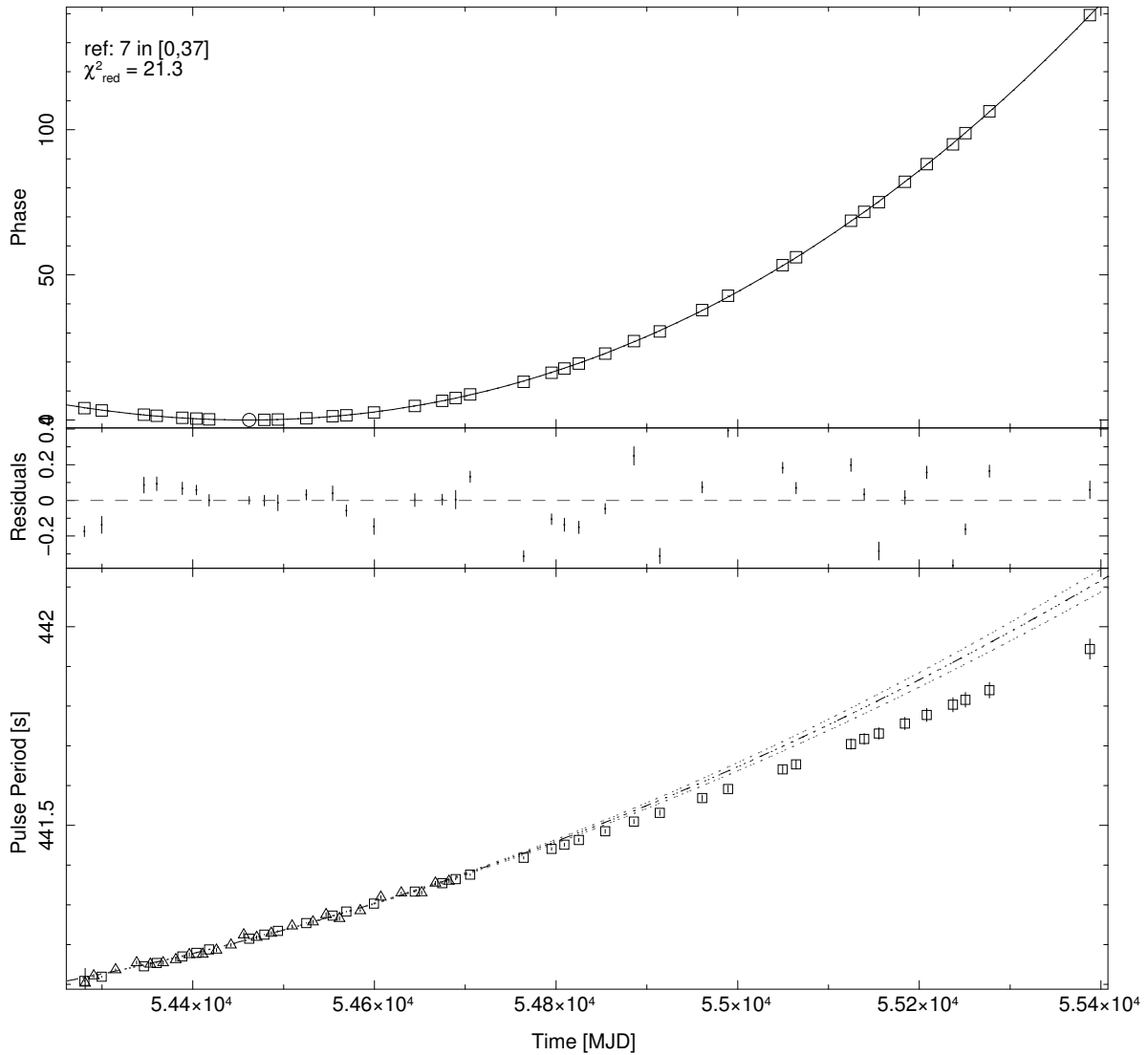


Figure 17: Model fit to the data configuration 7 in [0,37]. Top: Model fit (solid line) to the corrected $\Delta\Phi$ s (squares), the circle marks the reference point. Bottom: Resulting periods (squares) together with the periods calculated by Inam et al. (2009) (triangles) and the period evolution according the parameters shown in Tab.3. Detailed list of all values and fit parameter see appendix Table 7 and 8.

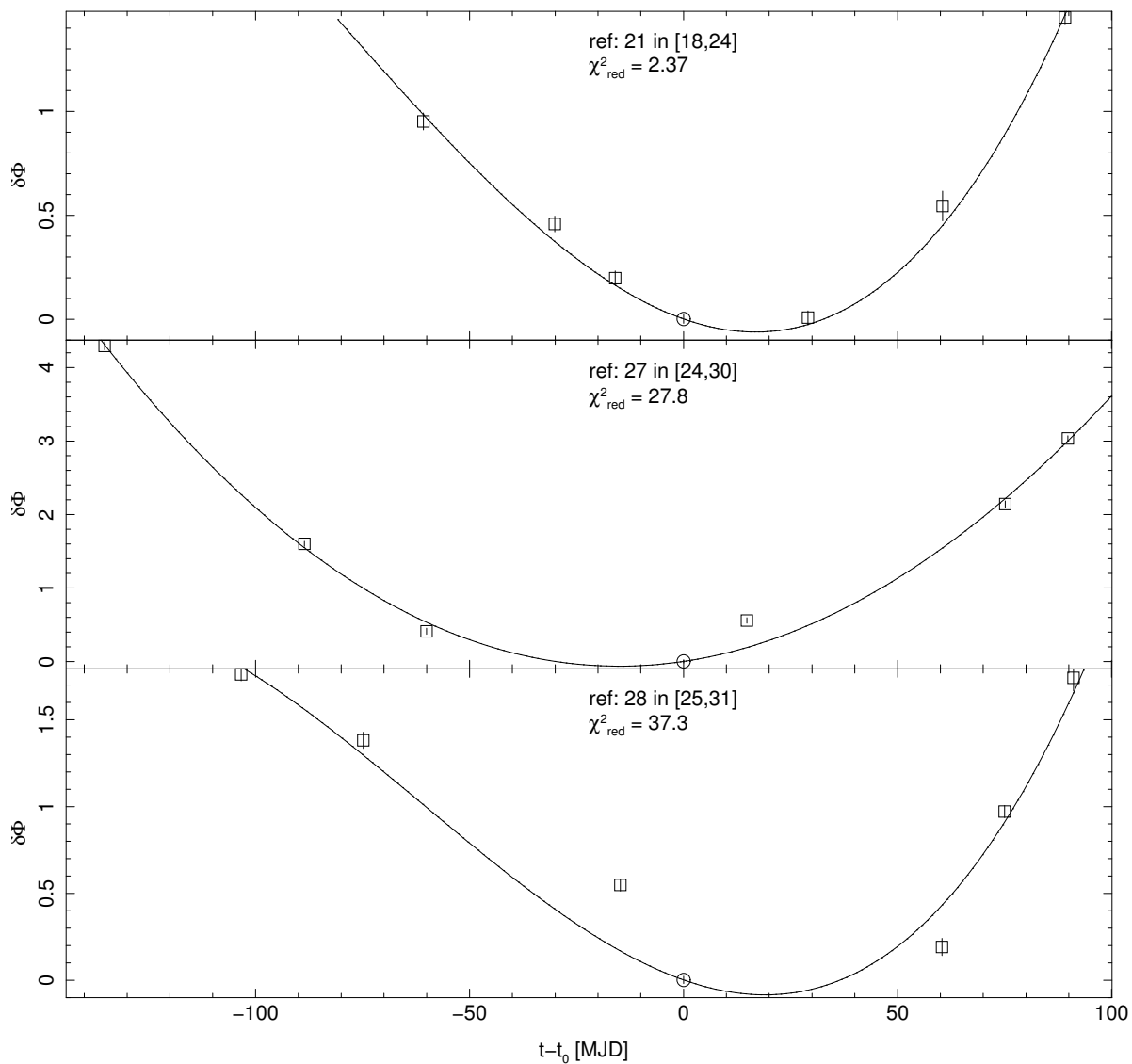


Figure 18: In all three graphs the attempt of fitting the model to a small data set of 7 data points each is shown. The solid line represents the model fit to the corrected $\Delta\Phi$ s (squares), the circle marks the reference point.

4.2 Automated phase correction

As the manual phase correction is very time-consuming it would not be possible to try several data configurations. Therefore an attempt to create a routine, which does that correction automatically, was done. As there are no references, which could help to fit a model to variable data points, each step of this routine was designed after the manual correction steps. In the followings a sketch of those steps is given:

1. The routine is given the wanted data configuration (reference point and data range), in which the two data points next to the reference are assumed to need no correction, which is a necessary criterion as with these three data points a fit is carried out. This also requires to have maximal 3 free parameter, which is fulfilled here as Φ_0 and t_0 are frozen. The resulting reduced chi square (χ_{red}^2) value is saved for further comparisons.
2. From there in every run through one new data point (uncorrected $\Delta\Phi$) alternating left and right with respect to the reference point is added. Afterwards an integer to this $\Delta\Phi$ is added until χ_{red}^2 is minimized again. This new χ_{red}^2 value overwrites the old value.
3. To check for a better correction and to correct mistakes, the point next to this last added data point is varied around its current position within $[-1, 0, 1]$ with respect to its current position. The restriction of the variation of this point to this interval was set as this phase correction value should be calculated accurate within this range due to step 2. For each of this variation the actual data point is varied (open range) until the minimal χ^2 value is found.
4. Then the routine goes back to the 2. step until all data points are added.

As it turned out it is advantageous to freeze $\dot{\nu} = 0$ at the beginning and when χ_{red}^2 reaches a certain value or a certain amount of data points with respect to the reference point is exceeded or all data points are added to unfreeze it. This proceeding prevents the routine to fit unlikely models with improper $\dot{\nu}$ values, as it is supposed to be vanishing small. This routine is an imitation of the steps, which are done manually to find suitable phase corrections and therefore its results are not reliable just like that. Also it is not technically mature, but it provides good results in most cases, especially if the $\Delta\Phi$ values are suitable and not like those examples shown in Figure 18.

This fitting routine was optimized to the model fits, which were done manually. That means this routine could reproduce those model fits, which were carried out with a manual phase correction.

4.3 Variation of the reference pulse period

Having the opportunity to fit an arbitrary amount of data configurations is the basic requirement for the approach to the reference period dependency problem. The idea of varying the reference period arise from the apparently condition that fitting the model to a data set based on an inaccurate reference period leads to poor models insofar that χ_{red}^2 increases the more P_{ref} deviates from the real value. Therefore the idea came up to variate P_{ref} around the first approximation calculated with the Inam fit parameter. The implementation of the variation of the reference pulse period is simple, P_{ref} is

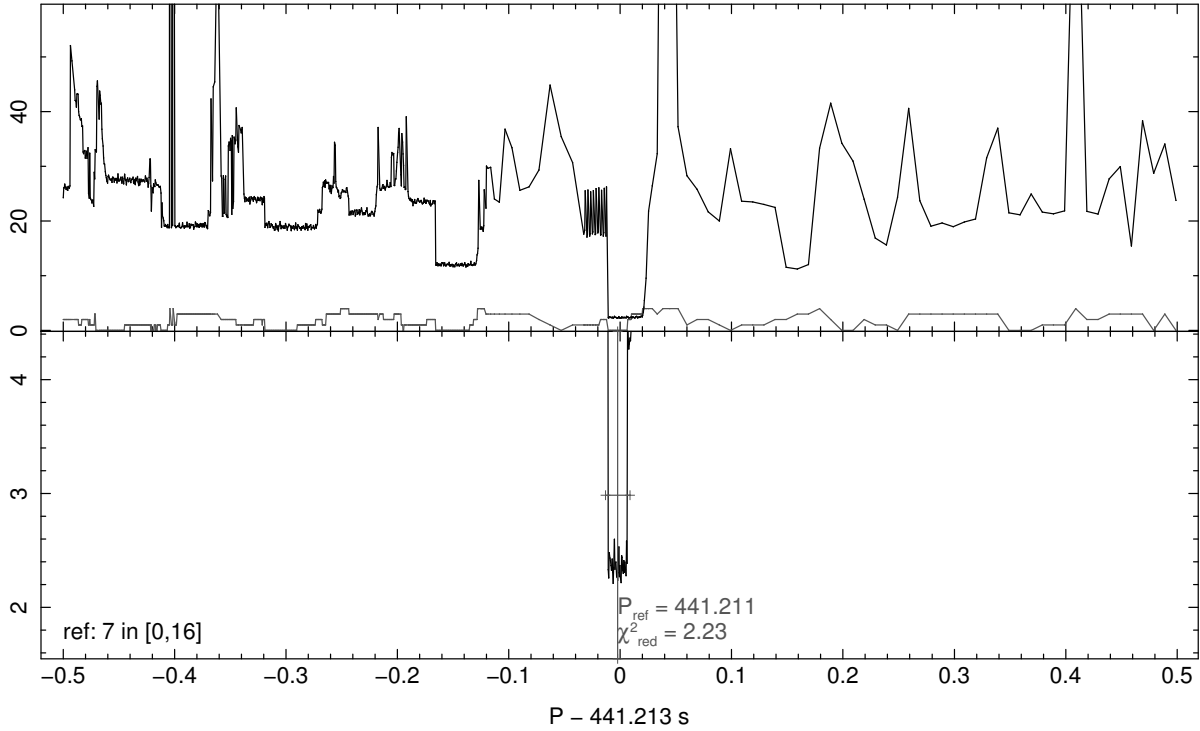


Figure 19: Variation of the reference pulse period using the data configuration with ref 7 in $[0,16]$ and a variation interval $[-0.5,0.5]$. In the top graph both selection criteria shown separately, χ_{red}^2 as black line and the additional criterion as gray line. Bottom graph shows the whole selection criterion together with the located reference pulse period and its error.

stepwise changed in a given interval. In every step a model fit with the automated phase correction algorithm is done. In the end the model with the lowest χ_{red}^2 value and the corresponding reference period is chosen.

This procedure, however, needs much cpu time as in each step several fits have to be calculated. Therefore the step size was calculated dynamically insofar that it was decreased if the current χ_{red}^2 value is smaller than all previous ones and increased if it is higher than the actual minimum of all previous χ_{red}^2 . Furthermore an additional selection criterion was implemented. This criterion depends on the phase correction values of the four data points closest to the reference point. More precisely the phase correction value Φ_{cor} of the two data point next to the reference point is double added to χ_{red}^2 and the next Φ_{cor} after those added once. The whole selection criterion is then: $\chi_{\text{red}}^2 + 2[\Phi_{\text{cor}}(\text{ref} - 1) + \Phi_{\text{cor}}(\text{ref} + 1)] + \Phi_{\text{cor}}(\text{ref} - 2) + \Phi_{\text{cor}}(\text{ref} + 2)$. The reason for this additional criterion is that χ_{red}^2 sometimes can be low even though the related model seems to be wrong. The assumption, that the closest phases ($\Delta\Phi$) do not need a phase correction or are preferably low, is also connected to the requirements of the phase connection method stated above.

In Figure 19 an example is shown for the Inam data set (ref 7 in $[0,16]$). The top panel shows the separated selection criteria and the bottom one shows their sum.

As the the region, in which the criterion is minimal with only little fluctuations, has a certain width, this width is taken as the error of the located reference pulse period, which is the middle of that region. Additional the step size is added to this error. This means that not the period with the minimal criterion value was taken itself, but that also values,

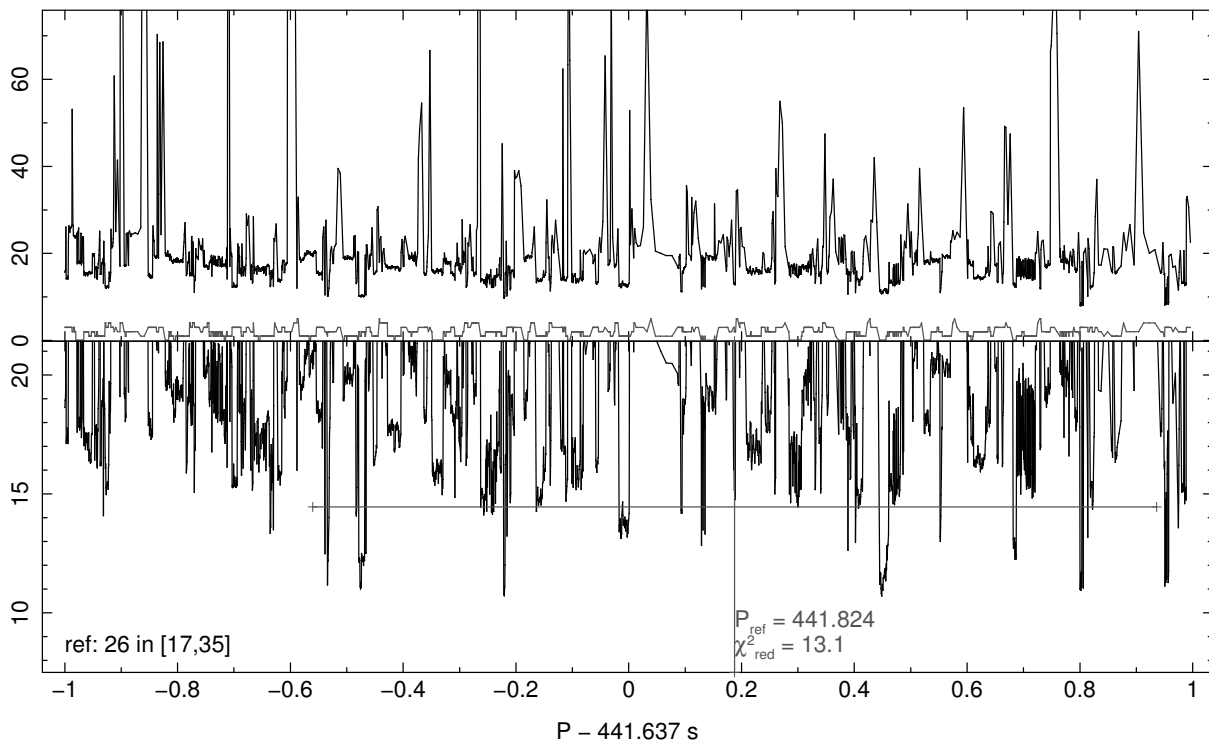


Figure 20: Variation of the reference pulse period using the data configuration with ref 26 in [17,35] and a variation interval $[-1, 1]$. In the top graph both selection criteria shown separately, χ_{red}^2 as black line and the additional criterion as gray line. Bottom graph shows the whole selection criterion together with the located reference pulse period and its error.

which slightly deviate from the minimum, were included. In this example the reference pulse period variation method worked well and also in other data configurations with the same reference point (obs. number 7). But there were also failures as shown in 20, in which no clear selection was possible. The huge estimated error is due to the many regions, which are within the allowed margin for the deviation from the minimal criterion value. Hence those huge errors indicate that the procedure failed. Interesting is that there was no model within the whole scanned interval with a low χ_{red}^2 value, although the automated fit routine seems to work for this data set, i.e. no unlikely values for the fit parameters were calculated.

Nevertheless this method was applied on a bunch of different data configurations with reference points within [2, 35] and a varying amount of data points within [5, 25] resulting in 374 different configurations, which also provides a better basement for statements. In Figure 22 all reference pulse periods, located with this method, are shown (diamonds). Also the pulse periods estimated by Inam et al. (2009) presented as triangles together with their period evolution (dashed and dotted lines) are shown. The solid line marks the range of the variation interval. At first glance it is a total disorder with no clear trend, especially within the epoch of the new observations. But removing the huge error afflicted points and having a closer look to the epoch of the old observations reveals a slightly different picture (Fig. 23). Out of the 374 points 125 are within this epoch, out of which 71 points (squares) are very close (within a window of ± 0.01) to the Inam model. That means more than 56% of the estimated reference pulse periods

are consistent with the measurements of Inam et al. (2009). On closer inspection it is conspicuous that many of the points deviate with the same value of $\sim \pm 0.15$ s from the expected pulse period for several MJDs. It almost looks like parallel lines to the Inam model. In most reference pulse period variations there are several secondary minima for χ_{red}^2 , occurring periodically with this value. In some cases one of this secondary minima seems to have a better χ_{red}^2 value, then that minimum, which actually corresponds to the real reference pulse period (example shown in Fig. 21). Hence it is a selection problem, which may can be solved by defining a better selection criterion.

Although this method is only a first attempt the results are an indicator that it is worthy for further investigations, especially as it provides a self-consistent test. This method primarily calculates only the best fitting reference pulse period for each data point, but additionally the corresponding fitted models are available. Therefore for several data points the result for the reference pulse period can be compared with their models, which should all overlap. The main problem is to provide a proper algorithm to fit the model to the data with an automated phase correction, which is the foundation of the reference pulse period variation. Also the selection criteria for the best reference period could be improved. Unfortunately this would go beyond the scope of this work.

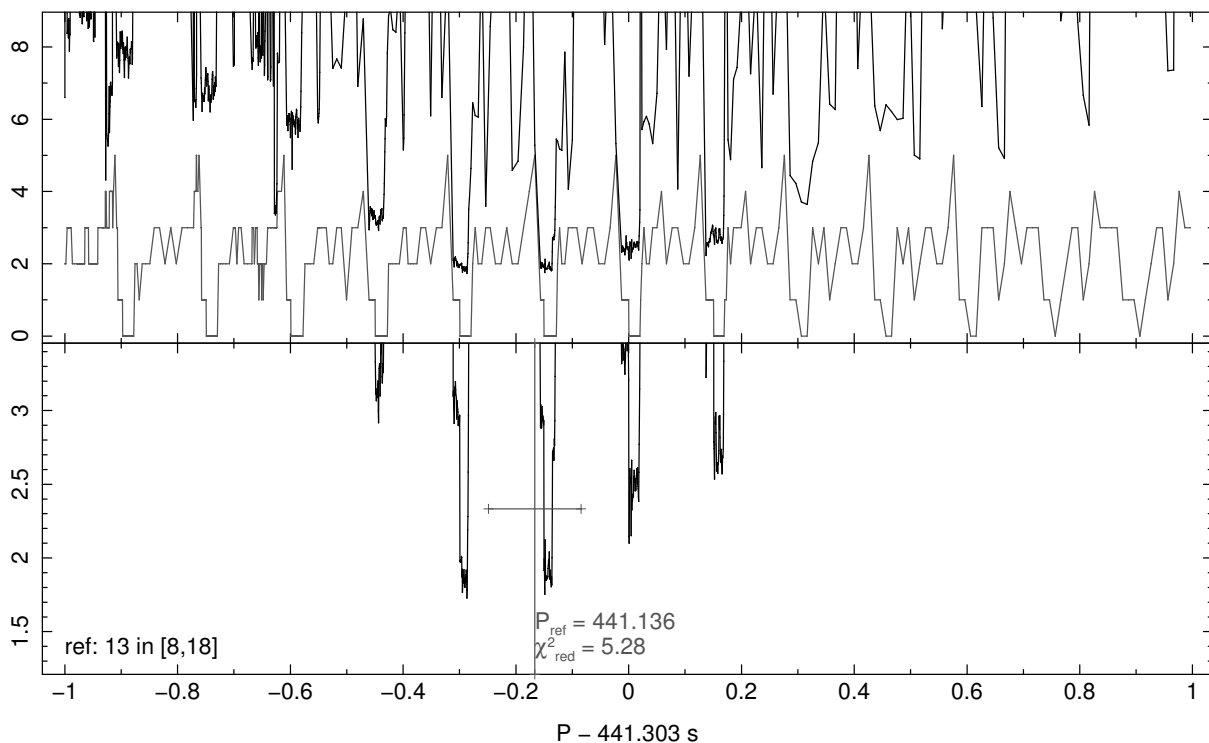


Figure 21: Variation of the reference pulse period using the data configuration with ref 13 in [8,18] and a variation interval $[-1, 1]$. In the top graph both selection criteria shown separately, χ_{red}^2 as black line and the additional criterion as gray line. Bottom graph shows the whole selection criterion together with the located reference pulse period and its error.

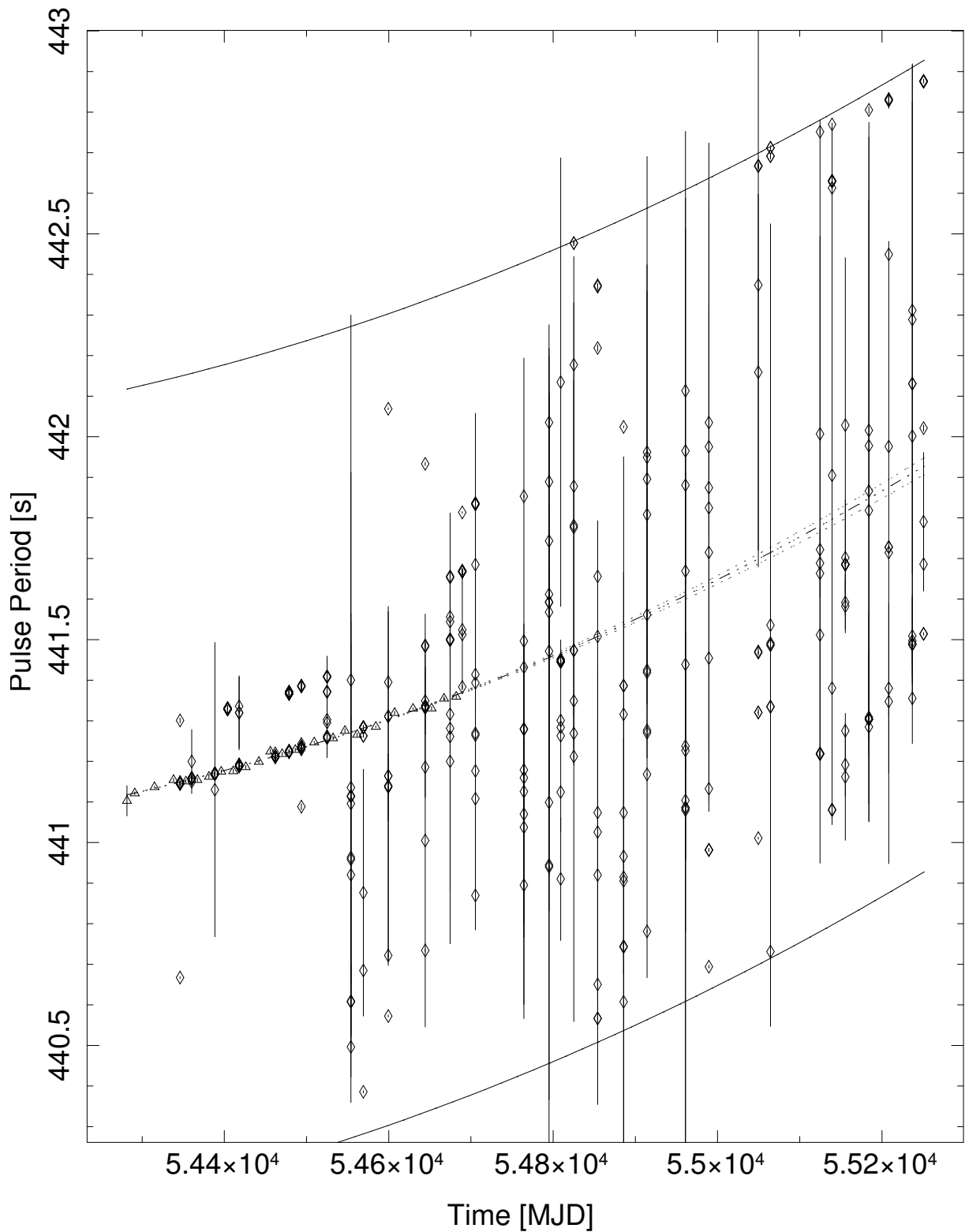


Figure 22: Overview of the results of the reference pulse period variation applied to different data configurations (diamonds). Inam pulse periods (triangles) and Inam model (dashed and dotted lines) are also shown for comparison. The solid line marks the variation interval.

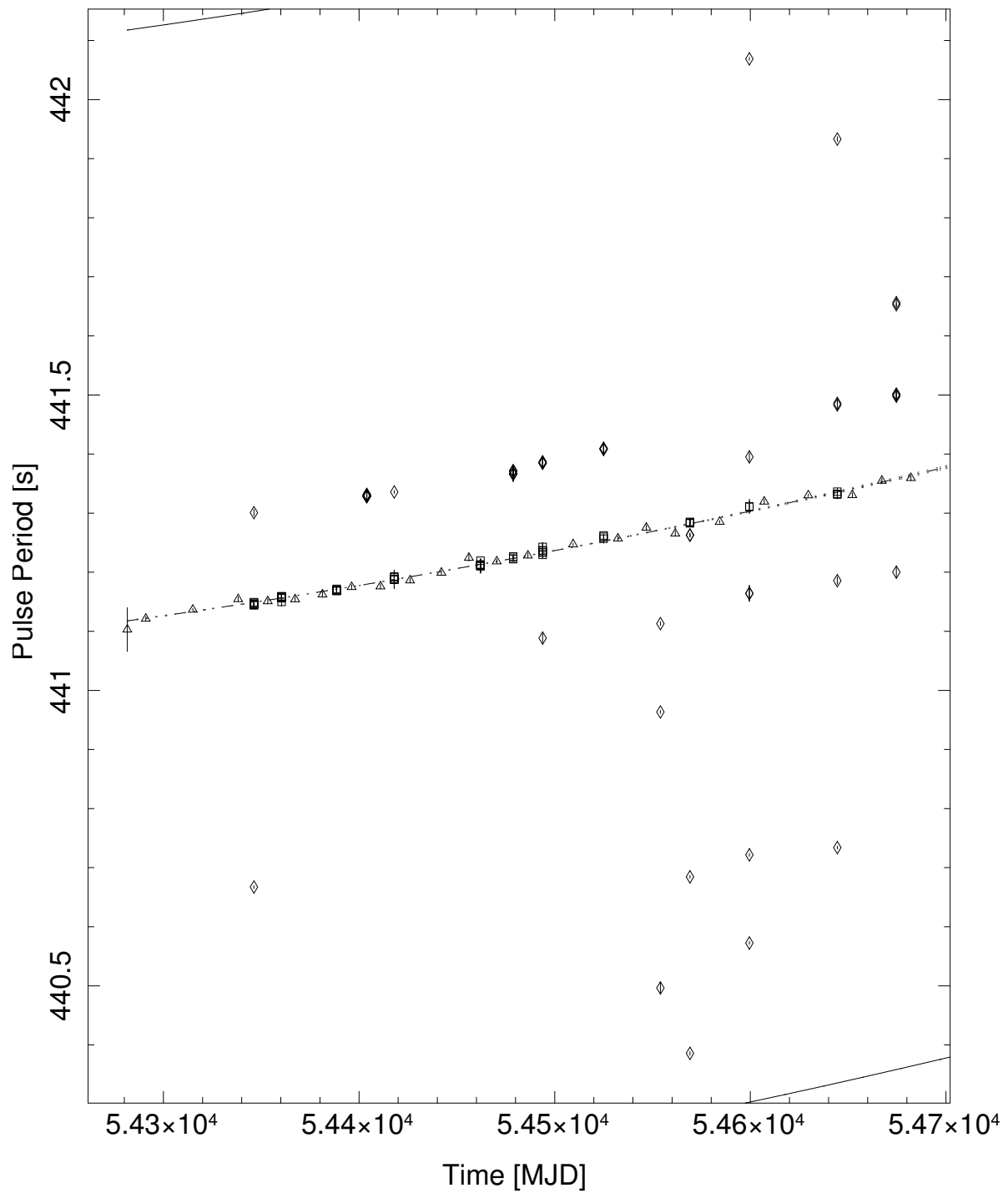


Figure 23: Out of the data points presented in 22 only those are shown, which are between 54682.1 MJD and 54281.5 MJD and have an error less than 0.05. Squares mark those points, which are within a range of ± 0.01 around the Inam model.

5 Conclusions

Unfortunately no reliable period evolution corresponding to the new observations can be provided. It is questionable if that evolution shown in Figure 17 is correct as the phase corrections are very high. No proper model, which is consistent with the measurements of Inam et al. (2009), could be found by using a reference pulse period within the newer observations. As there was no other possibility to calculate an accurate reference pulse period, it was estimated by using the Inam fit parameter. Therefore it is most likely that the predicted pulse period evolution of Inam and accordingly their model is not right for the time after 54682 MJD. That means that P , \dot{P} and also \ddot{P} have changed significantly. Also it is possible that one of those values increased and exceeded a critical point, which is beyond the limits of the phase connection method. It is likely that the changes occur at the transition to the new observation as already in this epoch no proper and consistent model was found.

The further attempts to find a reliable model by varying the reference pulse period support this conclusion as it provides to a certain degree consistent results to the Inam pulse periods, but only for the older observations. The reference pulse period variation method totally failed for the new observations. Drawing conclusions based on results of this method is not reliable as it is only a first attempt. But the presented results, however, would imply that there is either a huge jump in the pulse period, so that it is not within the set variation interval or the occurrence of major changes on short timescales as even for small data sets no suitable model was found. Looking at the pulse period history of 4U 1907 + 09 both scenarios would be untypical. Another torque reversal also could cause this results as the presented algorithm assumes that $\dot{P} > 0$.

In summary there must be a change in the binary system. The first thought may is, that there is a change in the mass accretion, which is one major reason for variations in the pulse period. But changes in the mass accretion would be connected to changes in the brightness visible in the lightcurve, which is note the case. Therefore the question for the reason of this changes cannot be answered, especially as it is not clear to date, which of the discussed accretion models applies to 4U 1907 + 09. Further investigations would help to determine the right accretion model, especially if there is really another torque reversal.

A Appendix

Table 4: Pulse period measurements of 4U 1907+09. Table from Inam et al. (2009).

Epoch (MJD)	Pulse Period (s)	Reference	Epoch (MJD)	Pulse Period (s)	Reference
45576	437.483±0.004	Makishima et al. (1984)	53121.1	441.274±0.005	Fritz et al. (2006)
45850	437.649±0.019	Cook & Page (1987)	53133.4	441.297±0.005	Fritz et al. (2006)
48156.6	439.19±0.02	Mihara (1995)	53253.6	441.224±0.010	Fritz et al. (2006)
50134	440.341±0.014	in 't Zand et al. (1998)	53291.3	441.201±0.005	Fritz et al. (2006)
50424.3	440.4854±0.0109	Baykal et al. (2006)	53314.0	441.188±0.005	Fritz et al. (2006)
50440.4	440.4877±0.0085	Baykal et al. (2001)	53324.7	441.183±0.005	Fritz et al. (2006)
50460.9	440.5116±0.0075	Baykal et al. (2006)	53443.4	441.154±0.005	Fritz et al. (2006)
50502.1	440.5518±0.0053	Baykal et al. (2006)	53473.3	441.139±0.005	Fritz et al. (2006)
50547.1	440.5681±0.0064	Baykal et al. (2006)	53503.8	441.124±0.005	Fritz et al. (2006)
50581.1	440.5794±0.0097	Baykal et al. (2006)	54281.5	441.1030±0.0372	Inam et al. (2009)
50606.0	440.6003±0.0115	Baykal et al. (2006)	54291.0	441.1213±0.0038	Inam et al. (2009)
50631.9	440.6189±0.0089	Baykal et al. (2006)	54315.0	441.1367±0.0021	Inam et al. (2009)
50665.5	440.6323±0.0069	Baykal et al. (2006)	54338.2	441.1545±0.0041	Inam et al. (2009)
50699.4	440.6460±0.0087	Baykal et al. (2006)	54353.3	441.1509±0.0046	Inam et al. (2009)
50726.8	440.6595±0.0105	Baykal et al. (2006)	54367.3	441.1543±0.0047	Inam et al. (2009)
50754.1	440.6785±0.0088	Baykal et al. (2006)	54381.3	441.1623±0.0046	Inam et al. (2009)
50782.5	440.6910±0.0097	Baykal et al. (2006)	54396.2	441.1750±0.0042	Inam et al. (2009)
51021.9	440.7045±0.0032	Baykal et al. (2001)	54410.9	441.1761±0.0047	Inam et al. (2009)
51080.9	440.7598±0.0010	Baykal et al. (2001)	54426.0	441.1862±0.0041	Inam et al. (2009)
51993.8	441.0484±0.0072	Baykal et al. (2006)	54442.1	441.1992±0.0040	Inam et al. (2009)
52016.8	441.0583±0.0071	Baykal et al. (2006)	54456.1	441.2245±0.0056	Inam et al. (2009)
52061.5	441.0595±0.0063	Baykal et al. (2006)	54470.4	441.2185±0.0039	Inam et al. (2009)
52088.0	441.0650±0.0063	Baykal et al. (2006)	54486.3	441.2284±0.0043	Inam et al. (2009)
52117.4	441.0821±0.0062	Baykal et al. (2006)	54509.4	441.2472±0.0021	Inam et al. (2009)
52141.2	441.0853±0.0082	Baykal et al. (2006)	54532.3	441.2537±0.0044	Inam et al. (2009)
52191.4	441.1067±0.0046	Baykal et al. (2006)	54546.8	441.2756±0.0046	Inam et al. (2009)
52217.2	441.1072±0.0077	Baykal et al. (2006)	54561.6	441.2657±0.0043	Inam et al. (2009)
52254.3	441.1259±0.0074	Baykal et al. (2006)	54584.3	441.2855±0.0022	Inam et al. (2009)
52292.0	441.1468±0.0065	Baykal et al. (2006)	54607.1	441.3195±0.0043	Inam et al. (2009)
52328.8	441.1353±0.0090	Baykal et al. (2006)	54629.6	441.3301±0.0022	Inam et al. (2009)
52739.3	441.253±0.005	Fritz et al. (2006)	54652.1	441.3307±0.0043	Inam et al. (2009)
52767.1	441.253±0.005	Fritz et al. (2006)	54667.2	441.3549±0.0044	Inam et al. (2009)
53083.9	441.283±0.005	Fritz et al. (2006)	54682.1	441.3596±0.0044	Inam et al. (2009)

Table 5: Overview of all available Observations. In the first column only for those observations numbers are given, which are selected to be good.

#	ObsID	Date [DD.MM.YYYY]	[MJD]	Duration [ks]	#PCU
0	93036-01-01-00	29.06.2007	54280.6	1.90	3
	93036-01-02-00	01.07.2007	54282.4	1.92	3
	93036-01-03-00	03.07.2007	54284.4	1.74	3
1	93036-01-04-00	18.07.2007	54299.6	1.76	3
	93036-01-05-00	02.08.2007	54314.3	1.74	1
	93036-01-06-00	18.08.2007	54330.4	1.69	2
2	93036-01-07-00	03.09.2007	54346.2	2.06	2
3	93036-01-08-00	17.09.2007	54360.4	1.55	3
	93036-01-09-00	01.10.2007	54374.2	1.68	2
4	93036-01-10-00	15.10.2007	54388.5	1.77	3
5	93036-01-11-00	30.10.2007	54403.9	2.76	3
6	93036-01-12-00	13.11.2007	54418.0	1.79	3
	93036-01-13-00	30.11.2007	54434.1	1.97	3
	93036-01-14-00	16.12.2007	54450.2	1.95	2
7	93036-01-15-00	28.12.2007	54462.1	1.66	3
8	93036-01-16-00	13.01.2008	54478.7	2.00	2
9	93036-01-17-00	28.01.2008	54493.8	1.42	2
	93036-01-18-00	13.02.2008	54509.3	1.34	2
10	93036-01-19-00	28.02.2008	54525.0	1.65	3
	93036-01-20-00	14.03.2008	54539.7	1.63	2
11	93036-01-21-00	29.03.2008	54554.0	1.20	2
12	93036-01-22-00	13.04.2008	54569.1	1.36	2
	93036-01-23-00	28.04.2008	54584.4	1.52	2
13	93036-01-24-00	13.05.2008	54599.5	1.84	2
	93036-01-25-00	28.05.2008	54614.7	1.58	2
	93036-01-26-00	12.06.2008	54629.3	1.92	2
14	93036-01-27-00	27.06.2008	54644.4	2.35	2
	93036-01-28-00	12.07.2008	54659.8	1.50	2
15	93036-01-29-00	27.07.2008	54674.6	1.57	2
16	93036-01-30-00	11.08.2008	54689.5	1.88	2
17	93036-01-31-00	27.08.2008	54705.4	1.77	3
	93036-01-32-00	10.09.2008	54719.8	0.73	1
	93036-01-33-00	25.09.2008	54734.0	1.76	1
	93036-01-34-00	10.10.2008	54749.1	1.92	2
18	93036-01-35-00	25.10.2008	54764.4	1.54	2
	93036-01-36-00	09.11.2008	54779.3	1.68	2
19	93036-01-37-00	25.11.2008	54795.1	1.95	2
20	93036-01-38-00	09.12.2008	54809.2	2.23	2
21	93036-01-39-00	25.12.2008	54825.1	1.66	2

Table 6: Continuation of Table 5.

#	ObsID	Date [DD.MM.YYYY]	[MJD]	Duration [ks]	#PCU
	94036-01-01-00	08.01.2009	54839.0	1.87	2
22	94036-01-02-00	23.01.2009	54854.2	1.37	2
	94036-01-03-00	07.02.2009	54869.4	1.06	2
23	94036-01-04-00	23.02.2009	54885.7	1.90	2
	94036-01-05-00	09.03.2009	54899.7	1.92	2
24	94036-01-06-00	24.03.2009	54914.3	0.94	1
	94036-01-07-00	08.04.2009	54929.0	1.10	1
	94036-01-08-00	23.04.2009	54944.6	2.05	2
25	94036-01-09-00	09.05.2009	54961.0	1.50	2
	94036-01-10-00	26.05.2009	54977.2	1.66	2
26	94036-01-11-00	07.06.2009	54989.5	1.80	1
	94036-01-12-00	21.06.2009	55003.5	2.16	2
	94036-01-13-00	05.07.2009	55018.0	1.15	2
	94036-01-14-00	21.07.2009	55033.1	1.95	2
27	94036-01-15-00	06.08.2009	55049.5	1.64	2
28	94036-01-16-00	21.08.2009	55064.3	1.81	2
	94036-01-17-00	06.09.2009	55080.2	1.75	1
	94036-01-18-00	20.09.2009	55094.3	1.92	1
	94036-01-19-00	05.10.2009	55109.6	1.45	2
29	94036-01-20-00	20.10.2009	55124.7	1.13	2
30	94036-01-21-00	04.11.2009	55139.3	1.61	2
31	94036-01-22-00	20.11.2009	55155.4	1.39	2
	94036-01-23-00	04.12.2009	55169.5	1.31	2
32	94036-01-24-00	19.12.2009	55184.1	1.92	2
33	95350-01-01-00	12.01.2010	55208.2	1.95	1
	95350-01-02-00	26.01.2010	55222.4	1.14	1
34	95350-01-03-00	09.02.2010	55237.0	1.84	2
35	95350-01-04-00	23.02.2010	55250.7	1.92	2
	95350-01-05-00	09.03.2010	55264.2	1.38	2
36	95350-01-06-00	22.03.2010	55277.3	1.12	2
	95350-01-07-00	03.04.2010	55289.7	1.93	2
	95350-01-08-00	20.04.2010	55306.1	1.26	2
	95350-01-09-00	02.05.2010	55319.0	1.35	2
	95350-01-10-00	15.05.2010	55331.4	1.92	2
	95350-01-11-00	31.05.2010	55347.5	1.90	1
	95350-01-12-00	12.06.2010	55359.8	2.06	1
	95350-01-13-00	26.06.2010	55373.0	1.12	2
37	95350-01-14-00	10.07.2010	55387.8	0.86	2

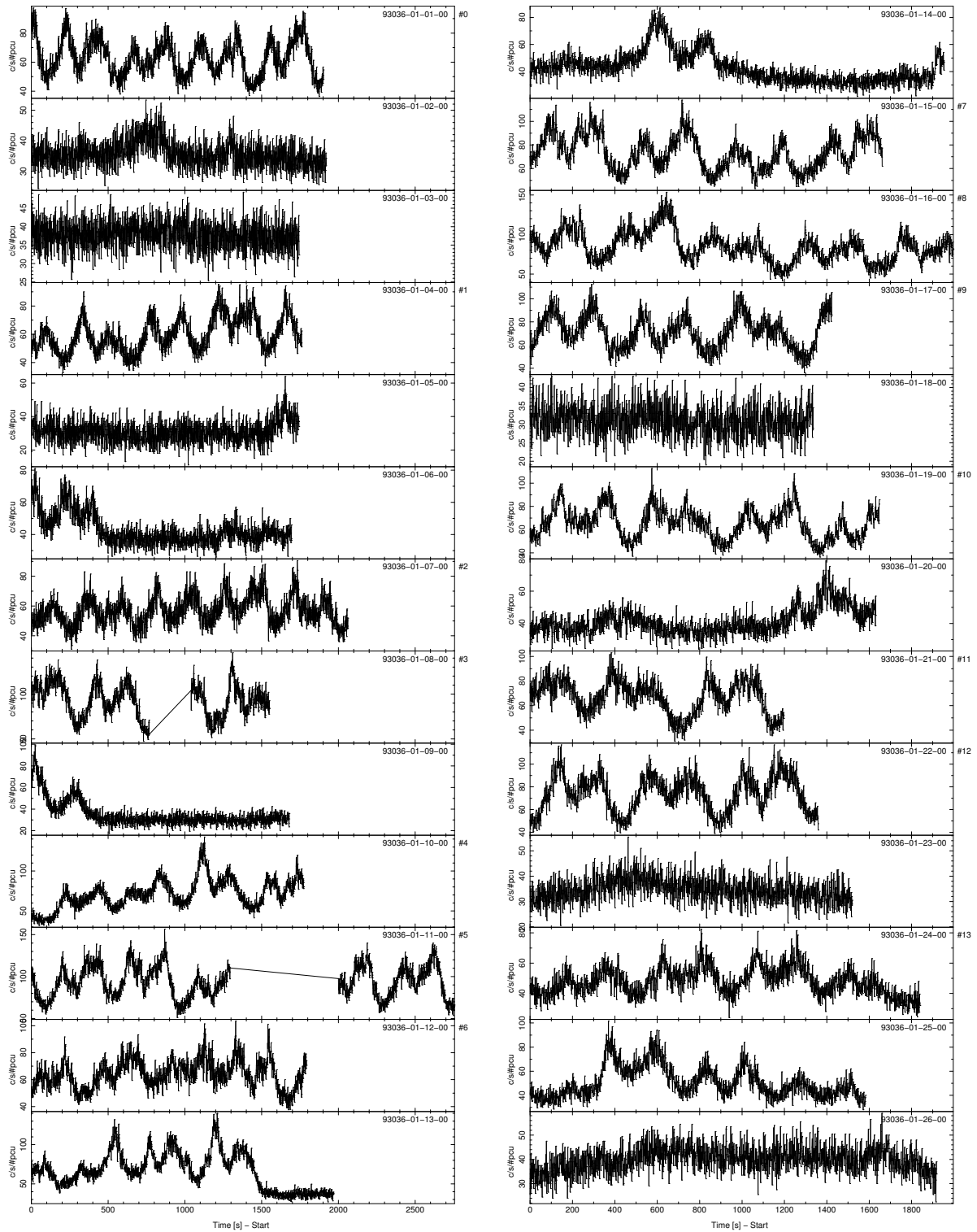


Figure 24: Light curves of all available Observations with binary and barycenter correction. Observation IDs are shown in the upper right corner. A number introduced with a '#' on the right of the graph indicates selected data.

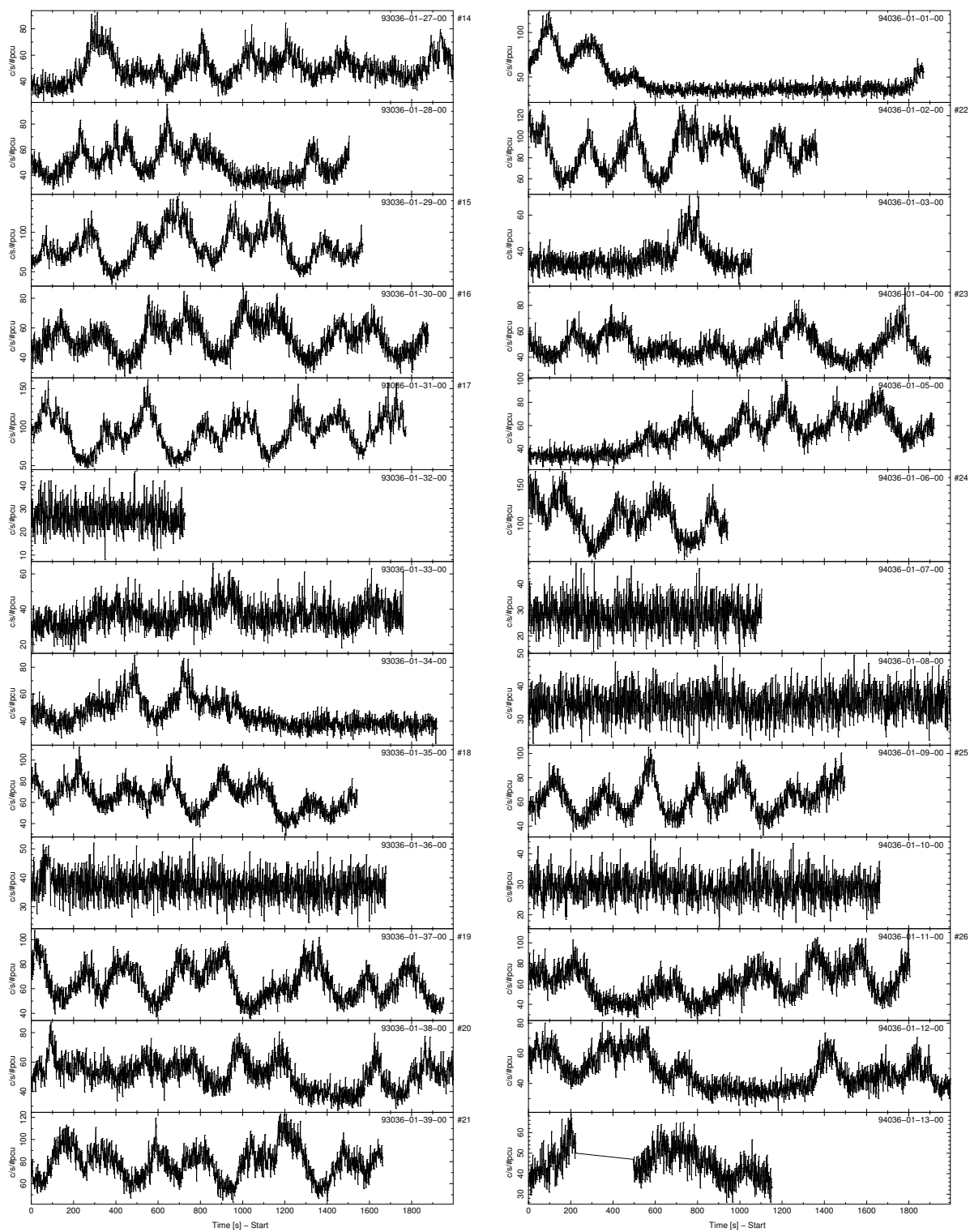


Figure 25: Continuation of Figure 24.

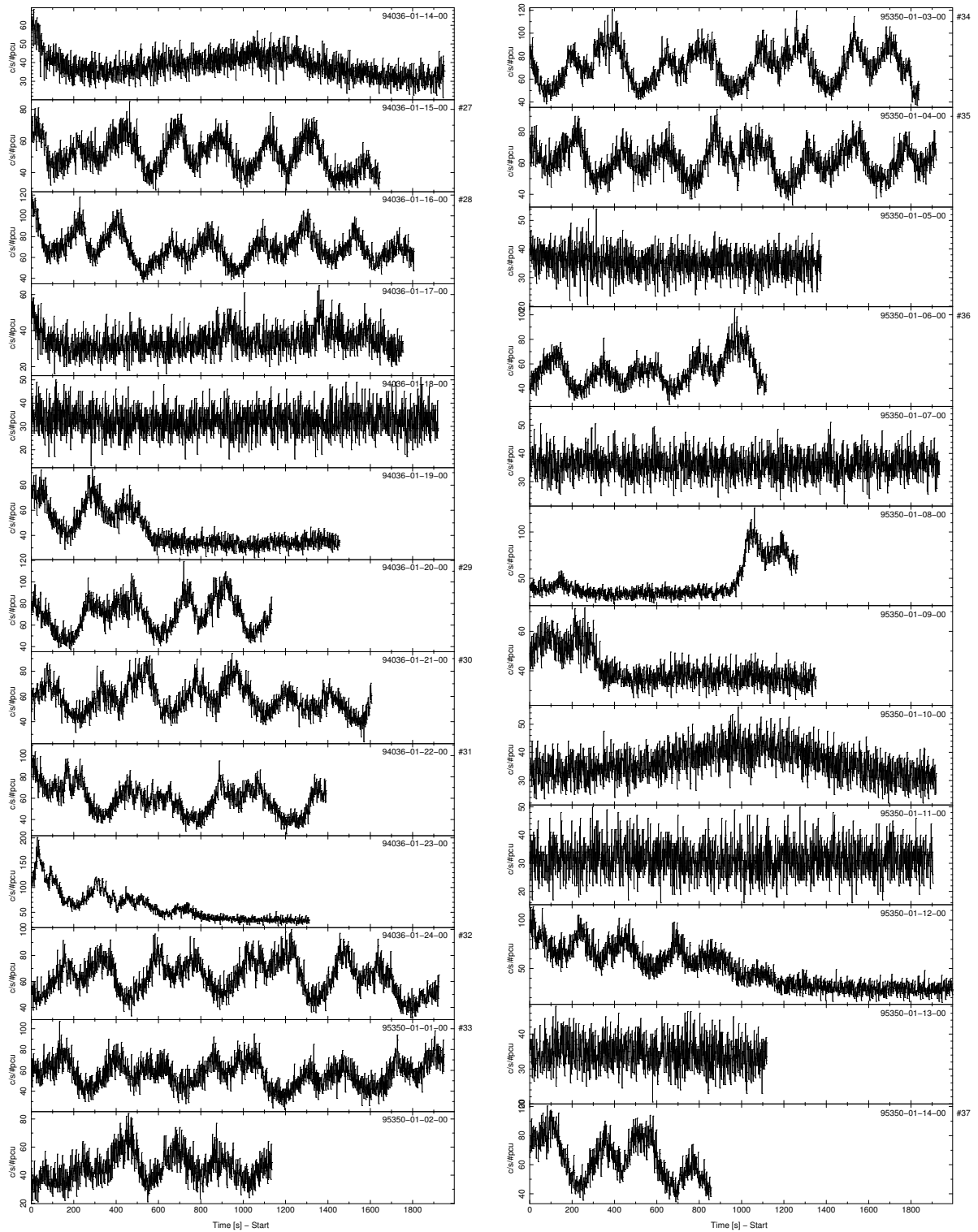


Figure 26: Continuation of Figure 24.

Table 7: List of the values shown in Figure 17.

#	MJD	$\Delta\Phi$	$\Delta(\Delta\Phi)$	Φ_{cor}	P [s]	ΔP [s]
0	54280.65	0.082	0.0296	4	441.108	0.0015
1	54299.63	0.278	0.0478	3	441.119	0.0013
2	54346.22	0.822	0.0439	1	441.145	0.0009
3	54360.36	0.428	0.0385	1	441.154	0.0009
4	54388.51	0.758	0.0349	0	441.170	0.0007
5	54403.94	0.485	0.0270	0	441.179	0.0007
6	54417.96	0.242	0.0326	0	441.188	0.0007
7	54462.06	0.002	0.0211	0	441.215	0.0006
8	54478.75	0.048	0.0296	0	441.225	0.0006
9	54493.80	0.145	0.0444	0	441.234	0.0006
10	54524.97	0.618	0.0290	0	441.254	0.0007
11	54554.02	0.275	0.0414	1	441.273	0.0008
12	54569.14	0.612	0.0319	1	441.283	0.0008
13	54599.49	0.595	0.0444	2	441.303	0.0010
14	54644.44	0.835	0.0360	4	441.334	0.0014
15	54674.61	0.585	0.0305	6	441.354	0.0017
16	54689.52	0.552	0.0514	7	441.365	0.0019
17	54705.44	0.788	0.0314	8	441.376	0.0021
18	54764.38	0.145	0.0306	13	441.418	0.0030
19	54795.06	0.295	0.0302	16	441.441	0.0036
20	54809.18	0.722	0.0364	17	441.451	0.0039
21	54825.15	0.435	0.0345	19	441.463	0.0042
22	54854.21	0.902	0.0293	22	441.485	0.0048
23	54885.66	0.158	0.0513	27	441.509	0.0056
24	54914.28	0.495	0.0429	30	441.532	0.0063
25	54960.98	0.855	0.0315	37	441.569	0.0076
26	54989.49	0.808	0.0359	42	441.592	0.0084
27	55049.55	0.328	0.0313	53	441.641	0.0104
28	55064.33	0.058	0.0322	56	441.653	0.0109
29	55124.70	0.648	0.0363	68	441.705	0.0131
30	55139.33	0.712	0.0324	71	441.717	0.0137
31	55155.44	0.042	0.0506	75	441.731	0.0144
32	55184.06	0.072	0.0389	82	441.756	0.0156
33	55208.20	0.138	0.0348	88	441.778	0.0166
34	55236.99	0.982	0.0326	94	441.804	0.0179
35	55250.70	0.812	0.0306	98	441.816	0.0185
36	55277.28	0.378	0.0338	106	441.840	0.0198
37	55387.77	0.485	0.0490	139	441.944	0.0254

Table 8: Result of the fitted model shown in Figure 17.

Parameter	Value	Error
Φ_0	1.667e-03	2.1076e-02
t_0 [MJD]	54462.06	0.01
$\delta\nu$ [Hz]	6.5743e-09	2.42185e-09
$\dot{\nu}$ [Hz s ⁻¹]	3.6770e-14	2.01506e-16
$\ddot{\nu}$ [HZ s ⁻²]	2.4968e-22	6.46815e-24

Table 9: List of the values shown in Figure 16.

#	MJD	$\Delta\Phi$	$\Delta(\Delta\Phi)$	Φ_{cor}	P [s]	ΔP [s]
0	54280.65	0.082	0.0296	4	441.116	0.0045
1	54299.63	0.278	0.0478	3	441.125	0.0038
2	54346.22	0.822	0.0439	1	441.148	0.0023
3	54360.36	0.428	0.0385	1	441.155	0.0020
4	54388.51	0.758	0.0349	0	441.171	0.0016
5	54403.94	0.485	0.0270	0	441.179	0.0015
6	54417.96	0.242	0.0326	0	441.187	0.0014
7	54462.06	0.002	0.0211	0	441.213	0.0013
8	54478.75	0.048	0.0296	0	441.223	0.0013
9	54493.80	0.145	0.0444	0	441.233	0.0014
10	54524.97	0.618	0.0290	0	441.253	0.0015
11	54554.02	0.275	0.0414	1	441.272	0.0018
12	54569.14	0.612	0.0319	1	441.282	0.0021
13	54599.49	0.595	0.0444	2	441.304	0.0029
14	54644.44	0.835	0.0360	4	441.336	0.0045
15	54674.61	0.585	0.0305	6	441.359	0.0060
16	54689.52	0.552	0.0514	7	441.371	0.0068

Table 10: Result of the fitted model shown in Figure 16.

Parameter	Value	Error
Φ_0	1.667e-03	2.1076e-02
t_0 [MJD]	54462.06	0.01
$\delta\nu$ [Hz]	-1.1139e-09	6.52772e-09
$\dot{\nu}$ [Hz s ⁻¹]	3.6018e-14	4.27841e-16
$\ddot{\nu}$ [HZ s ⁻²]	5.2135e-22	1.65232e-22

List of Figures

1	Double peaked orbital light curve	4
2	Stream model geometry	6
3	Fitted stream model	7
4	Accretion geometry	8
5	Accretion columns	9
6	Fan & pencil beam	9
7	Pulse period history of 4U 1907 + 09	10
8	Accretion model provided by Perna et al. (2006)	11
9	Schematic of RXTE spacecraft	13
10	Schematic of RXTE/PCA	13
11	Combined Lightcurves	16
12	Epoch fold & data selection	17
13	Epoch folds of selected data	19
14	Analysis method illustration	21
15	Phase correction	22
16	Analysis of ref 7 in (0,16)	25
17	Analysis of ref 7 in (0,37)	26
18	Model fit failure examples	27
19	Reference pulse period variation (a)	29
20	Reference pulse period variation (b)	30
21	Reference pulse period variation (c)	31
22	Reference pulse period variation: Overview (a)	32
23	Reference pulse period variation: Overview (b)	33
24	Light curves (a)	38
25	Light curves (b)	39
26	Light curves (b)	40

List of Tables

1	Binary orbit of 4U 1907 + 09	15
2	Selected Observations	18
3	Fit parameter	24
4	Pulse period measurements of 4U 1907+09	35
5	Observation Overview (a)	36
6	Observation Overview (b)	37
7	Value list (Fig.17)	41
8	Fit parameter (Fig.17)	42
9	Value list (Fig.16)	42
10	Fit parameter (Fig.16)	42

Bibliography

- Baykal A., C. IAli Alpar M., et al., 2001, *mnras* 327, 1269
- Baykal A., Inam S.C., Beklen E., 2006, *mnras* 369, 1760
- Becker P.A., Wolff M.T., 2005, *apjl* 621, L45
- Bondi H., Hoyle F., 1944, *mnras* 104, 273
- Cook M.C., Page C.G., 1987, *mnras* 225, 381
- Cox N.L.J., Kaper L., Mokiem M.R., 2005, *aap* 436, 661
- Davies S.R., 1990, *mnras* 244, 93
- Fritz S., 2008, Ph.D. thesis, Eberhard-Karls-Universität Tübingen
- Fritz S., Kreykenbohm I., Wilms J., et al., 2006, *aap* 458, 885
- Fürst F., Wilms J., Rothschild R.E., et al., 2009, *Earth and Planetary Science Letters* 281, 125
- Ghosh P., Lamb F.K., 1979, *apj* 234, 296
- Giacconi R., Kellogg E., Gorenstein P., et al., 1971, *apjl* 165, L27+
- in 't Zand J.J.M., Baykal A., Strohmayer T.E., 1998, *apj* 496, 386
- Inam S.C., Şahiner S., Baykal A., 2009, *mnras* 395, 1015
- Kostka M., Leahy D.A., 2010, *mnras* 407, 1182
- Kretschmar P., 1996, Ph.D. thesis, Universität Tübingen, Wilhelmstr. 32, 72074 Tübingen
- Kreykenbohm I., 2004, Ph.D. thesis, Eberhard-Karls-Universität Tübingen
- Kuster M., 2004, Ph.D. thesis, Universität Tübingen, Wilhelmstr. 32, 72074 Tübingen
- Larsson S., 1996, *aaps* 117, 197
- Leahy D.A., Darbro W., Elsner R.F., et al., 1983, *apj* 266, 160
- Leahy D.A., Kostka M., 2008, *mnras* 384, 747
- Makishima K., Kawai N., Koyama K., et al., 1984, *pasj* 36, 679
- Mihara T., 1995, Ph.D. thesis, , Dept. of Physics, Univ. of Tokyo (M95), (1995)
- Perna R., Bozzo E., Stella L., 2006, *apj* 639, 363
- Rivers E., Markowitz A., Pottschmidt K., et al., 2010, *apj* 709, 179
- Schwarzenberg-Czerny A., 1989, *mnras* 241, 153
- Smartt S.J., 2009, *araa* 47, 63
- Wilms J., 1998, Ph.D. thesis, Universität Tübingen, Wilhelmstr. 32, 72074 Tübingen

Acknowledgements

I would like to extend thanks to everyone who supported me during the time of this thesis. Special thanks go to

- I. Kreykenbohm and J. Wilms, as well as F. Fürst for much help and support.
- all the “Remeisen“ at the Dr. Remeis observatory in Bamberg, especially to Manfred Hanke, as well as, Moritz Böck and Tobias Beuchert.
- M. Müller and P. Hofmann for the helpful discussions and the moral support.

Erklärung

Hiermit bestätige ich, dass ich diese Arbeit selbstständig und nur unter Verwendung der angegebenen Hilfsmittel angefertigt habe.

Erlangen, 28.09.2010

Bastian Falkner